Zuza Andrew Vincent (Orcid ID: 0000-0001-6130-5121)

Odlum Margaret L (Orcid ID: 0000-0002-7873-9900)

Stockli Daniel Fritz (Orcid ID: 0000-0001-7652-2129)

Footwall rotation in a regional detachment fault system: Evidence for horizontal-axis rotational flow in the Miocene Searchlight pluton, NV

Andrew V. Zuza[1], Wenrong Cao[2], Nicholas H. Hinz[1], Joel W. DesOrmeau[2], Margaret Odlum[3], and Daniel F. Stockli[3]

(1) Nevada Bureau of Mines and Geology, University of Nevada, Reno, NV 89557

(2) Department of Geological Sciences and Engineering, University of Nevada, Reno, NV 89557

(3) Department of Geological Sciences, University of Texas, Austin, TX 78712, USA

*Corresponding author: azuza@unr.edu; avz5818@gmail.com

Submitted to: **Tectonics**

Submission date: **October 20th, 2018**

First manuscript revision: **March 6th, 2019**

2nd manuscript submitted: **May 14th, 2019**

3rd manuscript submitted: **June 10th, 2019**

ABSTRACT: The Miocene Searchlight pluton, exposed in the Colorado River extensional corridor of southern Nevada, tilted up to 90° on its side in the footwall of the east-directed Dupont Mountain detachment fault system. Rapid extension and rotation occurred immediately after the ca. 17-16 Ma emplacement of this 10×10 km granite-monzogranite body. To constrain the mechanism and timing of rapid footwall exhumation, we conducted detailed field, microstructural, electron backscatter diffraction (EBSD), and zircon (U-Th)/He (ZHe) and $^{40}Ar/^{39}Ar$ hornblende thermochronological analyses. Steeply dipping fabrics across this pluton formed over a range of temperature conditions, from magmatic to high- to low-temperature sub-solidus strain, and display distributed eastside-up shear. ZHe cooling ages are consistent with constraints from tilted volcanic strata and cross-cutting dikes that suggest initial rapid rotation (~75° Myr^{-1}) at 16.2-15.7 Ma followed by more modest exhumation rates until ca. 13 Ma. Our observations are used to test tilting models for the Searchlight pluton, including rigid-body rotation, antithetic imbrication, or flow-like rotation. Available observations are most consistent with a flow-like tilting mechanism. We present scaling analyses that highlight how footwall tilting-dominated extension more effectively cools the upper crust than pure-shear extension because the hottest deep materials exhumed rapidly toward the cooler surface. This extensional mechanism efficiently cools the upper crust, causing a negative feedback whereby the rapidly cooled crust becomes strong enough to halt further fast simple-shear extension. This may explain why rapid extension was transient and further extension is mostly accommodated by high-angle low-offset magnitude normal faults that developed in a colder stronger crust.

Introduction

Magmatism, deformation, and exhumation critically affect the regional geothermal profile, surface heat flux, and cooling history of the crust. The resulting thermal structures affect rheology, crustal differentiation, and growth of the continental lithosphere (e.g., Rudnick and Fountain, 1995; Paterson et al., 1998; Petford et al., 2000; Lenardic et al., 2000; Beaumont et al., 2001; Molnar et al., 2010; Rubin et al., 2017). These issues have been particularly well studied in contractional settings such as the Himalayan-Tibetan orogen and Gangdese arc, North American Cordillera and Sierran arc, Andean orogen and arc, and the arc root in Fjordland, New Zealand (e.g., Harrison et al., 2000; Miller and Paterson, 2001; Wen et al., 2008; DeCelles et al., 2009; Klepeis et al., 2010, 2016; Cao et al., 2016, 2019). Comparatively little research has focused on extensional domains (cf. Grocutt et al., 1994; Ehler et al., 2001; Grocutt and Taylor, 2002; Brun et al., 2018).

Rapid extension and the development of regional detachment fault systems exhume rocks from the middle crust toward the surface. The mechanisms responsible for exhuming footwall rocks, and the timing and rates of this process, affect the cooling history of continental crust, which in turn influences crustal rheology and strength because, to a first order, both strain rate and geothermal gradient affect crustal strength (Goetze and Evans, 1979; Molnar, 1992). Although thermo-mechanical modeling of different extensional modes (e.g., pure vs. simple shear) can quantify the thermal and topographic effects of lithospheric stretching (e.g., Buck et al., 1988; Buck, 1991; Rey et al., 2009), the kinematics of these processes are still debated, especially as they relate to field observations (e.g., Miller et al., 1983; Buck, 1988; Wernicke and Axen, 1988; Hamilton, 1988; Cooper et al., 2010; Platt et al., 2015).

The Colorado River extensional corridor (CREC) in southern Nevada is an exemplar of rapid large-magnitude extensional deformation to study the thermo-rheological evolution

of an extending crust with young and active magmatism and exhumation of deep, hot materials. Specifically, shortly after Miocene intrusion, the Searchlight pluton (Bachl et al., 2001) tilted up to 90° in the footwall of the east-directed Miocene Dupont Mountain detachment fault (Faulds et al., 2001, 2002a), and potentially records fabrics associated with this extensional process. The tilting mechanism of the Searchlight pluton has implications for (1) how different styles of crustal extension affect the regional thermal history and (2) the rheological evolution of the upper crust during relatively fast extension (strain rates of ~10^{-14} s^{-1}) (Gans and Bohrson, 1998).

In this contribution, we examined the nature of intra-pluton contacts and fabrics of the Searchlight pluton to investigate its exhumation-process and rates. This study involved regional-, outcrop-, and thin-section-scale structural observations, electron backscatter diffraction (EBSD) analyses, and zircon (U-Th)/He (ZHe) and $^{40}Ar/^{39}Ar$ hornblende thermochronometry to constrain the kinematics of this exhumation. Lastly, we present simple scaling analyses to investigate and discuss how fast extension and rapid exhumation of footwall rocks consisting of the recently intruded Searchlight pluton affect cooling rates and crustal strength along the Colorado River extensional corridor.

Geologic Framework

Regional extension since the Eocene(?)-early Miocene across the western United States (Hamilton and Myers, 1966; Stewart, 1978, 1980; Allmendinger et al., 1983) controls the present-day topography, physiography, hydrology, and economic resource distribution (e.g., ore bodies and geothermal-energy potential) across the area. Cenozoic extension initiated across two subparallel north-trending belts stretching from Canada to Mexico (Axen et al., 1993), and voluminous calc-alkaline magmatism was variably pre-, syn-, and post-extensional (e.g., Glazner and Bartley, 1984; Gans et al., 1989; Christansen and Yeats, 1992;

Axen et al., 1993; Faulds et al., 2001; Best et al., 2016). In the central Basin and Range (e.g., Wernicke and Snow, 1998), around the latitude of Las Vegas, NV, extension and magmatism initiated in the Miocene (e.g., Glazner and Bartley, 1984; Axen et al., 1993). The southern part of this extensional system is referred to as the Colorado River extensional corridor (CREC; e.g., Howard and John, 1987; Wernicke, 1992; Faulds et al., 2001) (**Fig. 1**). The northern CREC, which extends from Lake Mead in the north to the southern tip of Nevada in the south, is ~100-km-wide and highly extended (>100%) (**Fig. 1**) (e.g., Faulds et al., 1990, 2001). Here Miocene magmatism preceded extension, with both magmatism and extension propagating northward (Glazner and Bartley, 1984; Faulds et al., 2001). **Figure 1A** shows the migration of silicic magmatic centers from ca. 18.8 Ma in the south with the Silver Creek caldera (Ferguson et al., 2013) to ca. 13.1 Ma Wilson Ridge pluton (Honn and Smith, 2008) in the north near Lake Mead.

This study is focused on the Searchlight pluton, which is located in the southern Eldorado Mountains in the approximate middle of the northern CREC (**Fig. 1**). Miocene plutonism in this region, including Searchlight, was relatively short-lived over a ca. 1 Myr timescale from ca. 17 Ma to 16 Ma (e.g., Metcalf et al., 1995; Falkner et al., 1995; Cates et al., 2003; Miller et al., 2006; Johnson, 2014) (**Figs. 1A**). Regional extension across the southern Eldorado Mountains initiated during or immediately following the intrusion of the Searchlight pluton at ca. 16 Ma and ceased by 14-10 Ma, resulting in the present-day north-trending mountain-range morphology of the region (Anderson, 1971; Faulds, 1993, 1995; Faulds et al., 1994, 1995; Gans et al., 1994; Gans and Bohrson, 1998) (**Fig. 1**). Major extension at Searchlight's latitude was east directed along east-dipping normal faults. Just to the north there is a major transition to west-directed extension, and this transition is known as the Black Mountain accommodation zone (**Fig. 1B**) (Faulds et al., 1990; Faulds and Varga, 1998). The Searchlight pluton is bound on the west by the east-dipping McCullough Range

fault and the east by the shallowly east-dipping Dupont Mountain fault (**Figs. 1 and 2**) (e.g., Faulds et al., 2001, 2002a,b).

Volcanism started 1-4 Myr prior to regional extension and continued through the Miocene, although the intensity of volcanism dramatically decreased after ca. 15 Ma (Cole, 1989; Gans et al., 1989; Feuerbach et al., 1993; Smith and Faulds, 1994; Faulds et al., 1995; Gans and Bohrson, 1998; Ruppert, 1999; Dodge et al., 2005). **Figure 3** presents a local chronology of intrusive rocks based on existing geochronological constraints and field relationships.

Most of the granite to monzonite Searchlight pluton, its overlying volcanic rocks, and the sidewall/floor rocks have been mapped at 1:24,000 scale (Ruppert and Faulds, 1998; Faulds et al., 2002a,b, 2010; Hinz et al., 2012a,b). This mapping distinguished several intra-plutonic units, including the Upper (Ts_u), Middle (Ts_m), and Lower (Ts_l) pluton (Faulds et al., 2002a,b, 2010; Hinz et al., 2012a,b), which are further subdivided based on style of deformation or lithology (**Figs. 2 and 3**; **Table 1**). The Searchlight pluton (**Table 1**) intrudes Proterozoic basement gneiss, the Cretaceous two-mica Ireteba pluton (Kapp et al., 2002), and its own overlying volcanic pile (Faulds et al., 2001; Bachl et al., 2001). These intrusive contacts are observed along the pluton's paleo-roof, and side- and floor-walls (**Fig. 2**).

The Searchlight pluton is commonly viewed as having tilted 90° on its side. This is supported by the 80-90°W dips of the overlying Miocene volcanic rocks (Faulds et al., 2002a,b, 2001, 2010) and Al-in-hornblende crystallization pressure estimates (Hammarstrom and Zen, 1986; Anderson and Smith, 1995; corresponding depth estimates along the cross section in **Fig. 2C**). The estimated crystallization pressures, which correspond to a vertical depth, linearly correlate with the samples' horizontal map-view distance from the pluton-roof contact, corroborating approximately 90° tilting of the Searchlight pluton (e.g., Bachl et al., 2001; Miller and Miller, 2002; Miller et al., 2011) (**Fig. 2C**). The pluton's roof and floor

contacts are roughly vertical today, and restoration to a subhorizontal orientation requires 90° tilting. Note that many of the intra-pluton fabrics only dip up to ~70°W (**Fig. 2**), which may suggest that the internal part of the pluton rotated a different magnitude than its external contacts, although this observation remains unexplained.

The Cretaceous two-mica Ireteba pluton (Kapp et al., 2002) to the north of the Searchlight pluton is similarly tilted. The Ireteba pluton exposes a relatively distinct NNE-striking brittle-ductile transitional zone (BDT) at longitude ~114° 48.5'W that was mapped by previous workers on the basis of sub-solidus fabrics (Faulds et al., 2001; Hinz et al., 2012a, 2012b) (**Fig. 2**). To the west of this inferred BDT, the granite deforms via brittle mechanisms and to the east, it behaves ductilely (Faulds et al., 2001).

The Searchlight and Ireteba plutons are both crosscut by north-striking dikes that dip moderately east (**Fig. 2**) (Faulds et al., 2002a,b; Hinz and Faulds, 2009). This includes the ca. 15.5 Ma Eldorado dike swarm rocks that are abundant in the field area and dip ~40° east (**Fig. 2B**) (e.g., Hinz and Faulds, 2009; Hinz et al., 2012a). If these originally intruded vertically, they provide a tilt progression and suggest that the pluton had tilted ~50° by ca. 15.5 Ma.

Methods

We conducted an integrated field, microstructural, and thermochronological study across the Searchlight pluton (**Fig. 2**). Because the area has already been mapped at detail (**Fig. 2**), we focused our observations across important traverses, including along the (1) pluton sidewall, which is presently the northern pluton margin, (2) pluton-floor transition into the underlying Precambrian gneiss and Cretaceous Iretaba two-mica granite (i.e., the present-day eastern pluton margin), and (3) intra-pluton unit contacts and fabrics.

Microstructure analyses

Oriented samples were collected (**Fig. 2**) to compare the mineralogy, styles and inferred temperatures of deformation, and kinematics. Detailed petrographic analyses can yield semi-quantitative deformation temperatures that we also compared with EBSD analyses. Thin sections were cut parallel to lineations—often stretched plagioclase grains or linearly aligned mafic minerals—and perpendicular to foliations. Samples were described via petrographic microscope including the modal percentage of minerals, deformation microstructures observed within the grains and along their boundaries, and inferences of deformation temperatures based on mineral alignment, quartz and feldspar recrystallization textures, and internal grain structures (e.g., undulose extinction, myrmekite textures, mechanical twins, or sericite alteration).

EBSD analyses

The primary goal for EBSD analysis was to determine the quartz slip mechanism—as a proxy for deformation temperature—and shear sense (Krul and Vernon, 2005; Thigpen et al., 2010; Chapman et al., 2010; Zák et al., 2012; Law, 2014; Nevitt et al., 2017) to corroborate our petrologic observations. Polished thin sections underwent a final ~4 hour vibrational polish with 0.02 μm colloidal silica suspension to remove near-surface crystal lattice damage. EBSD maps were performed by collecting electron backscatter diffraction patterns from each node of a defined orthogonal grid using a Nordlys Nano high resolution detector and Oxford Instruments Aztec 3.0 acquisition software package on a JEOL 7100 FE-SEM housed in the Mackay Microbeam Laboratory at the University of Nevada, Reno (See **Supplemental Table 1** for run details regarding individual EBSD maps). Reconnaissance maps were first made using 10-30 μm stepsize and then focused analyses were conducted at 5

μm stepsize. Post processing used AZtecHKL software, which included removal of wild spikes and Dauphiné twin boundaries (Cross et al., 2017).

(U-Th)/He zircon thermochronology

(U-Th)/He thermochronology has been used successfully to understand the timing and thermal evolution in extensional settings by tracking exhumation and cooling of the footwall rocks (Axen et al., 2000; Stockli et al., 2000; Ehlers et al., 2003; Armstrong et al., 2004; Stockli, 2005; Bidgoli et al., 2015). In this work, we use zircon (U-Th)/He thermochronology (ZHe) to understand the thermal history of the Searchlight pluton, and relate this history to possible mechanisms for its exhumation. We chose ZHe because of the moderate closure temperature of the system (180-200ºC to as low as ~130ºC) (Reiners et al., 2002, 2004; Wolfe and Stockli, 2010; Guenthner et al., 2013; Colleps et al., 2018). Specifically, we aimed to constrain the cooling history of this pluton—intruded at approximately 750°C—as it was exhumed rapidly toward the surface. The ZHe system tracks cooling of rock through ~5-8 km depth (Wolfe and Stockli, 2010), depending on cooling rate, geothermal gradient, and zircon inclusions.

Zircons were separated from 7 samples (**Fig. 2**) using standard mineral-separation techniques at the University of Nevada, Reno. Analyses were performed on single-grain aliquots at the University of Texas at Austin using their laboratory procedures (e.g., Wolfe and Stockli, 2010; Singleton et al., 2014). We aimed for 5 aliquots per sample and used the (U-Th)/He practice of applying a single percentage error of 8% to all zircon analyses (Reiners et al., 2002). More detailed methods and (U-Th)/He zircon ages from individual analyses can be found in the Supplemental Materials. Weighted mean ZHe ages for each sample are provided in **Table 2**.

$^{40}Ar/^{39}Ar$ *hornblende thermochronology*

Hornblende $^{40}Ar/^{39}Ar$ thermochronology was conducted to assess the timing of higher temperature cooling of the Searchlight pluton. The effective closure temperature of $^{40}Ar/^{39}Ar$ hornblende analysis is ~500-550°C depending on cooling rate and grain properties (Harrison and McDougall, 1981; McDougall and Harrison, 1999). Two samples were collected from the lowermost pluton, at inferred paleodepths of ~8-12 km (Bachl et al., 2001): samples 13-4C (35.52691°N, 114.81745°W) and 15-2 (35.56765°N, 114.78263°W) (**Fig. 2A**).

Mineral separation and $^{40}Ar/^{39}Ar$ analyses were conducted at the Nevada Isotope Geochronology Lab at the University of Nevada, Las Vegas. Samples were irradiated at the U. S. Geological Survey TRIGA Reactor in Denver, CO, along with standard FC-2, a Fish Canyon Tuff sanidine (Renne et al., 1998). Detailed methods (e.g., Staudacher et al., 1978) and analytical data are in the Supplemental Materials.

Map- and Outcrop-scale Observations

The Searchlight pluton (**Table 1**) is crosscut by numerous mafic to felsic dikes (Bachl et al., 2001). Magmatic foliations and lineations are well developed across most of the pluton, although generally weaker in the western upper parts of the pluton than the eastern lower pluton (**Fig. 4**). Foliations generally strike north and dip west up to 90° (**Fig. 2**; **Supplemental Figure 4**). Previous workers assumed that magmatic fabrics were subhorizontal prior to tilting because these fabrics parallel intra-pluton contacts that presently dip 60-70° west and pluton-roof contacts that are subvertical, which are comparable to inferred rotation magnitudes and implies that these horizons were subhorizontal prior to tilting (Faulds et al., 2001; Bachl et al., 2001). This is consistent with the inference that some of the lower fabrics formed as magmatic state cumulates (Bachl et al., 2001), which would have developed as subhorizontal magmatic foliations. In outcrop, foliations are largely

defined by the alignment of elongate euhedral-subhedral minerals, such as feldspars and hornblende, most likely indicating some magmatic state origin (i.e., strain accumulated at magmatic temperatures above the solidus temperature) (**Fig. 4**). Microstructural observations suggest that much of magmatic state foliation is overprinted by sub-parallel sub-solidus strain (see the **Microstructural Observations** section below). Magmatic lineations are also observed across the entire pluton, and are comprised of aligned euhedral-subhedral hornblende or elongated plagioclase grains (**Fig. 4C**). They mostly plunge ~80-50° and trend west-northwest (~270-300°). Shear sense within the plutonic foliations, parallel to lineations, is weakly developed across most of the pluton and is primarily eastside-up as derived from recrystallized quartz tails, commonly in feldspar stress shadows, and S-C fabrics.

Flattened and sheared mafic enclaves are observed across the middle-to-lower pluton. They are commonly subparallel to magmatic and sub-solidus fabrics (e.g., Bachl et al., 2001), although we observed unit contacts truncating elongate enclaves (e.g., **Fig. 4B**). Their axial ratios are typically 1.5 to 4 (X/Z ratios), but we did not conduct systematic investigation of these enclaves because of their ambiguity as useful strain markers (Paterson et al., 2004). Intra-plutonic contacts (**Fig. 2; Table 1**) primarily demarcate mineralogical changes in the pluton and are gradational on a sub-meter scale (e.g., Bachl et al., 2001), but some are relatively sharp (**Fig. 4B**). There is no apparent shear gradient across these contacts and foliation attitudes do not change across these boundaries. Shear is observed broadly distributed between these contacts (e.g., primarily eastside up, although sometimes symmetric and coaxial), and they do not appear to be zones of higher localized shear.

The Dupont Mountain fault is exposed in the eastern part of the study area (**Figs. 2 and 4**). Here, Upper Searchlight and Miocene volcanic rocks are juxtaposed over strongly deformed Lower Searchlight monzodiorite and Cretaceous Ireteba pluton. At one location, the fault dips ~35°E with east-trending striations and footwall stretching lineations (**Fig. 4D**).

A cataclastic fault zone overprints a mylonitic fabric in the footwall. Both display top-east shear as evidenced by Riedel shear fractures and S-C fabrics, consistent with the inferred east-directed transport of the Dupont Mountain fault (Faulds et al., 2001; **Fig. 2**). The footwall rocks within ~100 m of the fault display pervasive east-dipping top-east shear related to this fault. The shear planes in the footwall rocks progressively change dip from east-dipping, to subhorizontal, and to west-dipping moving west into the Searchlight Ts_{ld} unit. The west-dipping fabrics parallel most of the fabrics across the Searchlight pluton to the west, or upward through the pluton (**Fig. 2**). Moving away from the mapped Dupont Mountain fault over a distance of ~150 m the kinematics also change from top-east, associated with Dupont Mountain shear, to bottom-east, top-west, which parallels the shear kinematics observed distributed throughout the pluton that are not associated directly with shear on the Dupont Mountain fault. **Figure 4E** shows asymmetric boudinage and S-C fabrics that suggest top-west, bottom-east shear along subhorizontal planes. In another outcrop, Ts_{ld} intruding a relatively rigid block of undeformed gabbro displays strong sub-solidus shear fabrics indicative of eastside-up motion (**Figs. 4F-4H**). We interpret that eastside-up shear affected this outcrop, with the more felsic and weaker Ts_{ld} deforming while the gabbro remained rigid, translating along this local shear zone.

Field and map observations of the Dupont Mountain fault (Ruppert and Faulds, 1999) show that it truncates bedding at a high angle, and these steep cutoff relationships provide constraints on the original orientation of this fault as it cut the Searchlight pluton. For example, in the Fourth of July Mountain quadrangle, in the southern map area, Miocene volcanic rocks make up the hanging wall of the Dupont Mountain fault, which are juxtaposed as a klippe over steeply tilted Proterozoic gneiss and ~18.8 Ma Peach Springs Tuff (Glazner et al., 1986; Ferguson et al., 2013). Specifically, the subhorizontal Dupont Mountain fault crosscuts Peach Springs Tuff that dips ~80°W (Ruppert and Faulds, 1999), which requires a

footwall cutoff angle of comparable dip. Similar steep fault cutoffs were observed for the McCullough Range fault (**Fig. 2**) (Faulds et al., 2002b), which imply the fault initiated at a steep angle.

Most of fabrics across the pluton have consistent parallel west-dipping attitudes, except near the pluton's paleobase in the east and along the northern pluton-wallrock boundary (**Fig. 2**), which we expand upon in the following paragraphs. In the east, the foliations of the lowermost unit are folded in north-trending antiform-synform pairs, probably because the fabrics were locally drag-folded during interaction with the subhorizontal-to-east-dipping Dupont Mountain fault (**Fig. 2**). These folds result in dip variability (**Fig. 2**), and cause the fabrics to roll over toward the east and dip more gently to become parallel to the Dupont Mountain fault (Faulds et al., 1996, 2001; Bachl et al., 2001). For example, at one location near the pluton base (near sample 15-1, **Fig. 2**), foliations dip east, but shear-sense indicators still show eastside-up shear. We interpret that these rocks were tilted by this localized folding, which explains their east-dip but similar eastside-up shear sense. Near sample 13-2 (**Fig. 2**), sub-solidus shear in Searchlight rocks dipping ~55-60°W is eastside up. However, shallow outcrop-scale brittle faults, dipping ~20°NW, crosscut these fabrics and show southeast-directed motion. We interpret that this late-stage brittle deformation was related to southeast-directed shear of the Dupont Mountain fault.

Along the northern contact between the Searchlight pluton and wallrock, fabrics of the pluton are folded against the wallrock, which consists of Proterozoic gneiss (**Fig. 5**). Here, foliations generally dip northwest but define a ~1-km wavelength asymmetric tight fold with a NW-plunging axis. The rocks observed here are strongly lineated, and lineations parallel this fold axis (see stereonet in **Fig. 5A**). Kinematics observed at the outcrop- and thin-section-scales show southeast-side-up shear, which is shear of the pluton-side up to the south-southeast relative to the wallrock (**Fig. 5**). Based on the pervasive pluton-up shear in this

structure and the parallelism between the fold axis and transport direction, defined by the stretching lineations, we interpret this structure as a kilometer-scale *a*-type fold, in which the fold hinge parallels the transport direction, also known as an <a> fold (e.g., Mattauer, 1975; Malavieille, 1987; Hacker et al., 2000) (**Fig. 5**). Alternatively, this could be interpreted as a sheath fold (Cobbold and Qinquis, 1980; Carreras et al., 2005), but Quaternary cover hinders more observations of the structure (**Fig. 5**). Either way, our observations are consistent with the interpretation that this structure accommodated motion of the pluton up to the southeast relative to the northern wallrock, as illustrated in **Figure 5B** as an *a*-type fold.

Microstructural Observations

The following guidelines were used to determine magmatic state versus sub-solidus fabric formation. When fabrics form in a magmatic state, crystal alignment is facilitated by the melt lubricant in the suspension flow resulting in shape preferred orientation for euhedral-subhedral magmatic minerals, including hornblende, plagioclase, and biotite. Primary magmatic textures, such as plagioclase growth twinning and oscillatory zoning, are commonly preserved. Magmatic fabrics lack intra-crystalline strain and dynamic recrystallization, which commonly appear in sub-solidus fabrics. Fabrics formed below the solidus temperature typically show features of crystal-plastic deformation, including intra-crystal strain such as undulatory extinction and mechanical twinning as well as inter-crystal deformation including varies types of dynamic recrystallization such as grain-boundary migrations or quartz-tail formation around porphyroclasts (Passchier and Simpson, 1986; Paterson et al., 1989; Paterson et al., 1998).

Over typical geologic strain rates, mechanisms of quartz recrystallization dominantly vary as a function temperature during sub-solidus deformation. Typically for quartz recrystallization, **bulging recrystallization (BLG)** occurs at ~250-400°C, **subgrain rotation**

(SGR) occurs at higher temperatures up to 400-500°C, and at >550-500°C **grain boundary migration (GBM)** dominates (e.g., Jessell, 1987; Blumenfeld et al., 1986, 1988; Mainprice et al., 1986; Hirth and Tullis, 1992; Lloyd and Freeman, 1994; Stipp et al., 2002; Law, 2014). Feldspar recrystallization occurs at greater temperatures than quartz and shows signs of **BLG** at ~450-600°C and **SGR** at temperatures >500°C (Tullis and Yund, 1985, 1991; Tsurumi et al., 2003). If sub-solidus deformation occurred below the crystal-plastic deformation temperature, micro-faulting and fracturing will be observed. Fracturing of feldspar grains is common at temperatures below 500°C (Passchier, 1982; Pryer, 1993). In the samples, continuous overprinting of magmatic fabrics by progressively cooler sub-solidus fabrics was observed, indicating that the deformation took place before full crystallization of the pluton and continued into sub-solidus temperatures.

We describe in detail six representative samples from across the Searchlight pluton (**Fig. 6**). Samples are dominated by feldspar grains, with generally more alkali feldspar than plagioclase. However, in the sample description below based on optical microscopy we did not differentiate feldspars because this study is mostly concerned with deformation textures and plagioclase and alkali feldspars tend to deform similarly (e.g., Tsurumi et al., 2003). All samples show an alignment of euhedral and subhedral magmatic minerals suggesting the existence of magmatic state strain. Microstructural analysis reveals that most of the samples are also overprinted by sub-parallel sub-solidus strain. The intensity of this overprinted sub-solidus strain varies, and we describe samples in order from most intense sub-solidus strain to least. One caveat to our descriptions is that the samples with apparently less sub-solidus strain also contain less quartz, which makes interpreting medium temperature sub-solidus strain and overall kinematics more difficult. **Figure 6** shows representative photomicrographs from these samples.

Sample 14-4 is a granitoid mylonite collected from the northern margin of the Searchlight pluton in the lower-lower unit (**Figs. 2 and 6**). The sample is strongly lineated and foliated in hand sample. It consists of feldspar (~64%), quartz grains and longer quartz ribbons (30%), biotite (4%), and subhedral-anhedral hornblende (~2%) with minor zircon and sphene. Magmatic state strain observed in this sample is represented by the alignment of euhedral-subhedral hornblende, biotite, sphene, and plagioclase with albite twinning. The highest temperature (>600°C) submagmatic to sub-solidus deformation is evidence by abundant myrmekite recrystallization of feldspar with core-mantle structure (e.g., Tsurumi et al., 2003), quartz GBM recrystallization with coarse-grained strain-free monomineralic quartz ribbons (~100-150 μm in size) with smooth grain boundaries. High- through medium-temperature (600-400°C) deformation is mainly recorded via quartz GBM and SGR recrystallization, feldspar undulose extinction, "flame-shaped" lamellae in plagioclase, and BLG recrystallization in feldspar. The mix of recrystallized grains of quartz and plagioclase results in polyphase fine-grained aggregates of quartz (~50-60 μm) and feldspar (~20 μm) grains. Lower temperature deformation (300-400°C) is evidenced by quartz BLG recrystallization and feldspar alteration to sericite. Brittle fractures are observed crosscutting feldspar grains, antithetic to shear sense (**Fig. 6**).

Kinematics observed from brittle fractures and asymmetric tails of recrystallized tails associated with feldspar porphyroclasts indicates eastside-up shear (i.e., top toward lineation trend 277°) (**Fig. 6**), although there are some, relatively fewer, ambiguous indicators showing opposite kinematics. Eastside-up shear for this sample is further supported by EBSD analyses discussed later. We interpret this sample to have experienced continuous deformation from magmatic temperatures through high- to low-temperature sub-solidus deformation. Compared to the other samples, this mylonitic sample shows more pervasive higher temperature sub-solidus strain.

Sample 14-3 was collected ~100 m to the southeast from sample 14-4, also from the lower-lower Searchlight unit (**Figs. 2 and 6**). The sample is very strongly lineated with less well-developed foliations. It consists of feldspar (~75%), quartz (~15%), and subhedral biotite (~5%) and hornblende (~5%) with minor sphene. Elongated feldspar grains define the lineation and aligned hornblende and feldspar define foliation.

Magmatic state strain is represented by the alignment of euhedral to subhedral hornblende, biotite, and feldspar with growth twinning and zoning. Compared to **Sample 14-4**, this sample displays less myrmekite and less SGR recrystallization of feldspar near the grain margins, which overall suggests less sub-magmatic to highest-temperature sub-solidus strain (>600°C). High- to medium-temperature (600-400°C) strain is mostly evidenced by feldspar BLG recrystallization and quartz SGR recrystallization. Lower temperature strain (300-400°C) is shown by mechanical twinning and sericite alteration of feldspar as well as BLG recrystallization and undulose extinction of quartz.

The shear kinematics show primarily southeast-side-up shear (i.e., away from lineation trend 300°) on the basis of biotite fish imbrication (**Fig. 6**), which yields similar kinematics to **Sample 14-4**. We interpret that this sample also experienced continuous deformation from magmatic temperatures to low-temperature sub-solidus deformation.

Sample 15-1 was collected from the northeast corner of the Searchlight pluton, near the junction of the pluton's paleo-wall- and floor-rock (**Fig. 2A**). This (quartz)monzodiorite unit is the deformed lowermost Searchlight pluton, and is intermingled with Proterozoic gneisses and sheared Ireteba pluton. This sample comes from a localized region that is folded by ~100-m-wavelength north-trending antiform-synform pairs, and unlike the other samples, sample 15-1 is east-dipping with east-plunging lineations. Based on field observations, we interpret this to have been folded to the east relative to the other samples as a result of motion

along the Dupont Mountain fault; the trace of this fault surface is <1 km east from this sample location.

This sample consists of feldspar (~60%), quartz (~30%), biotite (6%), and hornblende (4%) with minor euhedral sphene. As with the other samples, magmatic state strain is evidenced by alignment of euhedral to subhedral magmatic hornblende, biotite, sphene, and plagioclase with twinning. Sub-magmatic to highest temperature (>600°C) sub-solidus strain is recorded by a relatively few myrmekite textures, minor SGR recrystallization of feldspar, some quartz GBM recrystallization, and chessboard subgrains in quartz grains suggesting the simultaneous activation of basal <a> and prism <c> slip systems. High- to medium-temperature (600-400°C) deformation is observed with feldspar BLG recrystallization, some myrmekite texture, and minor quartz SGR recrystallization (**Fig. 6**). Medium- to low-temperature (< 400°C to 300°C) sub-solidus strain is mainly represented by quartz undulose extinction. This sample also shows more low-temperature deformation, including retrogression of hornblende and biotite, pressure solution, and calcite-infilled cracks in feldspar grains. We interpret that this sample experienced continuous deformation from magmatic state to lower-temperature sub-solidus strain but more strain accumulated at lower temperatures when compared with the other samples. Since this sample is closer to the pluton-wallrock contact than other samples, it may have cooled more quickly from magmatic temperatures and thus recorded lower temperature sub-solidus strain. Observed kinematics from recrystallized quartz tails in the shadows of larger feldspar grains indicate eastside-up motion, despite the samples different east-dipping attitude on the eastern limb of a north-trending antiform (**Fig. 2A**). Unfolding this outcrop parallel to the rest of the Searchlight pluton to the west would result in a west dip with similar eastside-up shear.

Sample 13-2 is a (quartz)monzodiorite collected from near the paleo-base of the Searchlight pluton, along its easternmost extent (**Figs. 2A and 6**). This unit was mapped as

the deformed, lowermost Searchlight pluton, and is strongly foliated. Magmatic lineations defined by aligned feldspar were variably observed in outcrop. This sample consists of feldspar (80%), quartz (8%), hornblende (8%), and biotite (4%). Magmatic state strain is recorded by aligned feldspar, hornblende, biotite, and sphene. Submagmatic to highest temperature (>600°C) sub-solidus strain consists of myrmekite and chessboard subgrains in quartz. Feldspar grains do not typically show SGR recrystallization; however, minor BLG recrystallization is observed. Compared to other samples, feldspar grain boundaries are relatively sharp. Quartz also largely lacks extensive SGR recrystallization. This suggests that the high- to medium-temperature (600-400°C) strain is relatively weakly developed in this sample. Medium- to low-temperature (< 400°C to 300°C) sub-solidus strain is represented by quartz BLG recrystallization and undulose extinction, mechanical twinning, brittle cracks, and sericite alteration in plagioclase.

Kinematics from this sample are inferred to be eastside-up based on asymmetric quartz tails formed in stress shadows around feldspar grains (i.e., top toward lineation trend 280°) (**Fig. 6**). We interpret that this sample experienced continuous deformation from magmatic temperatures to low-temperature sub-solidus deformation, with the less evidence for higher temperature sub-solidus strain than most of the other observed samples.

Sample 14-6 is a quartz monzonite that was collected from the lower-lower unit of the Searchlight pluton, away from the pluton's margins and base (**Fig. 2**). In outcrop, strong magmatic foliations defined by aligned biotite, hornblende, and feldspar grains were observed. The sample consists of feldspar (75%), quartz (~10%), hornblende (~9%), and biotite (~6%), with minor sphene and zircon. Magmatic state strain is represented by aligned euhedral to subhedral grains and especially the crystal-preferred orientations (CPO) in plagioclase. Submagmatic to the highest temperature (>600-700°C) sub-solidus strain is evidenced by quartz chessboard subgrains, some myrmekite texture, and quartz GBM

recrystallization as evidenced by interlobate quartz boundaries (**Fig. 6**). High- to medium-temperature (600-400°C) strain is recorded by local BLG recrystallization along generally smooth feldspar margins. Medium- to low-temperature (< 400°C to 300°C) sub-solidus strain is mainly represented by quartz undulose extinction, brittle fracturing in feldspar, and the alteration of hornblende and biotite. Kinematics in this sample are ambiguous. Overall, compared to other samples, this sample shows primarily magmatic state strain that is less overprinted by sub-solidus strain.

Sample 185 is a granite from the middle Searchlight collected just west of the contact with the lower Searchlight (**Fig. 2A**). A faint magmatic fabric was observed in outcrop dipping 68°W, as evidenced by aligned subhedral hornblende and biotite. The sample consists of feldspar (78%), interstitial quartz (~7%), biotite (~7%), hornblende (~6%), and euhedral large 1 mm sphene (~2%). Magmatic state strain is recorded by the alignment of biotite and hornblende, and minor chessboard subgrains in quartz suggest high-temperature (>600°C) sub-solidus strain. Feldspar shows common BLG-SGR recrystallization along its grain boundaries and quartz GBM demonstrates sub-solidus strain at ~600°C+ to 500°C. Lower temperature (300-400°C) sub-solidus strain is evidenced by mechanical twinning and brittle fractures in the feldspar grains and undulose extinction in quartz. Kinematics are ambiguous in this sample. The sample is similar to sample 14-6 in that it shows primarily magmatic state strain with subtle overprinting sub-solidus strain.

In summary, all samples show magmatic state fabrics overprinted by some degree of sub-solidus strain over a wide range of temperatures (**Fig. 6**). Magmatic fabrics generally show little discernable asymmetry or shear strain, and thus may reflect coaxial strain (Faulds et al., 2001) at higher temperatures. Sub-solidus quartz recrystallization reveals eastside-up shear in most samples, although some are relatively ambiguous (i.e., samples 14-6 and 185).

We note that this strain does not manifest itself as concentrated discrete high-strain shear zones, but appears to represent distributed shearing.

EBSD Results

We conducted EBSD analyses on four samples (i.e., 13-2, 15-1, 14-4, and 14-3; **Fig. 2A**); results are summarized in **Figure 7**. Thin-section-scale maps were not useful for this study because of the overprinting deformation and recrystallization textures. Other studies of plutonic fabrics spanning the transition from magmatic to sub-solidus strain show complicated c-axis EBSD results (e.g., Žák et al., 2012). Accordingly, we focused on small-scale analyses of recrystallized quartz domains. Results are presented as inverse-pole figure (IPF) maps with corresponding color-coded c-axis pole figures. Contoured *c*-axis pole-figure plots of one analysis per quartz grain were generated to avoid orientation bias toward larger grains (**Fig. 7**).

Sample 13-2, collected from the deformed lowermost Searchlight pluton (**Fig. 2A**), shows variable c-axis distributions. The dominant c-axis maxima suggest rhomb <a> slip at ~400-500°C, and the observed asymmetry (off the z-axis) suggests eastside-up shear (**Fig. 7A**). Some poles are concentrated near the Y-axis (i.e., plot's center), suggesting prism <a> activity (Lister and Dornsiepen, 1982; Law, 1990) indicative of medium- to high-temperature (~500-600°C) strain (**Fig. 7A**). Some grains show a c-axis maxima near the X-axis, indicative of prism <c> slip at relatively high temperatures (Mainprice et al. 1986; de Araújo et al. 2003) (**Fig. 7A**). Microstructural quartz textures suggest a mix of SGR and GBM, which corroborates the quartz slip systems interpreted from the EBSD analyses. Sample 15-1, also collected from deformed lowermost Searchlight pluton (**Fig. 2A**), shows basal <a> activity at lower temperatures (300-400°C) that are corroborated by BLG-SGR recrystallization observations (**Fig. 7B**). The asymmetric c-axis suggests top-west shear.

For sample 14-4 (**Fig. 2A**) we focused on recrystallized quartz grains and a long quartz ribbon (**Fig. 7C**). The quartz ribbon displayed a strong peripheral c-axis maxima near 45° from the foliation (**Fig. 7C**), which may have resulted from combined activity of basal <a>, rhomb <a+c>, and prism <c> slip (Mainprice et al., 1986; Stipp et al., 2002; Schulmann et al., 2008). The recrystallized quartz grains show basal <a> activity at lower temperatures (300-400°C) that match SGR-BLG recrystallization textures observed in these grains (**Fig. 7C**). Quartz grains from sample 14-3 (**Fig. 2A**) display a c-axis maxima centered predominately along the Y-axis, suggesting prism <a> activity at medium- to high-temperatures (~500-600°C) (**Fig. 7D**). A weak sub-maxima plotted near the Z-axis and suggests rhomb <a> activity in the 400°C to 500°C range. Relatively weak asymmetry of this sub-maxima suggests eastside-up shear (**Fig. 7D**). These EBSD results are consistent with observations made from microstructural observations previously outlined.

Thermochronology Results

(U-Th)/He zircon thermochronometry

Mean ZHe ages and standard deviations from each sample are reported in **Table 2**. Individual grain analyses that yielded ages that are older than the intrusion age of the Searchlight pluton and related igneous rocks (ca. 17-16 Ma; e.g., Johnson, 2014) were excluded from our mean ZHe age calculations. Samples had three or more replicates to produce a mean age, except for sample SLP2, which only had two after excluding an outlier analysis.

ZHe age interpretation can be complicated by radiation damage to the zircon-crystal lattice (Hurley and Fairbairn, 1952; Reiners et al., 2002, 2004; Nasdala et al., 2004; Reich et al., 2007). A strong negative correlation of ZHe age and effective U concentrations (i.e., eU) implies stronger radiation damage (Reiners, 2005; Guenthner et al., 2013; Orme et al., 2016).

Because our ages do not display such correlation (**Supplemental Figure 1**), we expect that our samples were not affected by considerable radiation damage. Thus, the obtained average ZHe ages represent the time at which the samples cooled through an effective closure temperature range of ~180°C to 200°C (e.g., Reiners et al., 2002h, 2004; Wolfe and Stockli, 2010; Guenthner et al., 2013; Colleps et al., 2018). Furthermore, the lack of age-eU correlations in all samples suggests that the samples moved rapidly through the partial retention zone (PRZ).

Weighted mean ZHe ages span ca. 12.3 Ma to 16.4 Ma (**Table 2**), which are <4 Myr younger than the crystallization age of the Searchlight Pluton (i.e., ca. 17-16 Ma). Alone, these ages suggest cooling of the pluton shortly after emplacement from a solidus temperature (>700°C) through ZHe closure temperatures of ~180-200°C.

$^{40}Ar/^{39}Ar$ hornblende thermochronology

The two samples analyzed for $^{40}Ar/^{39}Ar$ hornblende ages were collected from the lower Searchlight pluton (**Fig. 2A**). The sampling rationale was that the thermal history of these originally deep rocks should provide crucial information regarding the tilting and cooling process of the Searchlight pluton. In the simplest case, the deeper rocks should cool slowly because they have the smallest temperature gradient in comparison to the wallrock and background geothermal gradient. However, based on pre-tilting geometries and AlHb barometry estimates, these samples presumably travelled the farthest to reach the surface from their original positions in the middile crust.

Neither sample yielded a perfect plateau age, but we visually determined a qualitative plateau age for each sample. The total gas age and visually determined plateau age for sample 13-4C are ca. 17.1 Ma and ca. 16.4 Ma respectively (**Supplemental Figure 3**). The total gas age and visually determined plateau age for sample 15-2 are ca. 16.7 Ma

and ca. 16.9 Ma respectively (**Supplemental Figure 3**). We interpret that a meaningful and conservative age range for samples 13-4C and 15-2 are ca. 17.1-16.4 Ma and ca. 16.9-16.7 Ma, respectively. Johnson (2014) provided two sensitive high-resolution ion microprobe zircon ages from the same lower Searchlight unit with a ^{207}Pb common lead correction. The weighted mean ^{206}Pb/^{238}U zircon ages are 16.7±0.2 Ma and 16.3±0.4 Ma (Johnson, 2014), which together have a weighted average of 16.6 ± 0.4 Ma. Therefore, our hornblende argon age overlaps assumed crystallization ages for the lower Searchlight pluton.

Discussion

Kinematic cooling model for zircon helium ages

Robust interpretation of the ZHe ages requires an assumed kinematic model to link with vertical exhumation of the rock samples. **Figure 8** shows the setup of our model. Because the Searchlight pluton tilted up to ~90° on its side (Bachl et al., 2001), we assume that samples collected along the Earth's surface were original oriented vertically (**Fig. 8A**). The depth that each sample is below the Earth's surface, l, varies as a function of time due to rotation. This depth can be evaluated by the following relationship:

$$l(t) = R\cos(\omega t) \quad (1)$$

where l is measured in the z direction (down is positive z), R is the distance of the sample from the rotational center in profile view, which here is the Earth's surface, ω is the rotation rate, and t is the time since the start of pluton rotation, such that $\omega t = \theta$ if ω is constant (**Fig. 8C**). The rotational center is placed at the present-day western extent of the Miocene volcanic rocks that overlie the Searchlight pluton (**Fig. 2**), which would have been at the Earth's surface before rotation. Prior to extension and tilting, these volcanic rocks were ~2-km thick over the pluton-volcanic rock contact. Therefore, R equals the distance of our samples from the western margin of the Searchlight pluton along a N74°E line—the cross-section line (**Fig. 2A**)—plus ~2 km (**Table 2**).

We estimate the ZHe ages of samples of different R values, assuming that the rocks started initially below the PRZ. The effective ZHe closure depth (D_c) can be obtained by dividing effective ZHe closure temperature $T_{\text{eff\_cl}}$ by the geothermal gradient $\frac{dT}{dz} = \Gamma$ (**Fig. 8**):

$$D_c(T_{\text{eff\_cl}}, \Gamma) = \frac{T_{\text{eff\_cl}}}{\Gamma} \quad (2)$$

If we let l=D_c, we obtain the time at which a sample passes through D_c. Setting equation (1) equal to equation (2) yields:

$$t\left(T_{\text{eff\_cl}}, R, \Gamma, \omega\right) = \frac{\cos^{-1}\left(\frac{T_{\text{eff\_cl}}}{R\Gamma}\right)}{\omega} \quad (3)$$

The predicted ZHe age of a sample equals the starting time minus t above; we here assume a ca. 16.2 Ma rotation initiation. **Figure 9A** shows synthetic plots with the predicted ZHe age given R values for a range of rotation rates, closure temperatures (190±10ºC), and geothermal gradients. Lower rotation rates shifts each curve toward a younger cooling age because the sample will exhume more slowly through the PRZ.

Figure 9B plots the raw ZHe data as a function of age and distance from an inferred rotation point R. Overlain on this plot are R-ZHe age predictions based on an assigned parameter set following equation (3). Note all of the ZHe samples were initially below the effective closure depth of the ZHe system. The ZHe ages plot between rotation-rate outlines of 10° Myr^{-1} and 25° Myr^{-1} (**Fig. 9B**), which suggests the ZHe ages of these samples can be explained approximately by constant-rate rotation of the Dupont Mountain footwall at a rate of ~15-20° Myr^{-1}. This would result in bulk 90° rotation in 4.5-6 Myr, which agrees with published observations suggesting regional extension lasted from ca. 16 Ma to 14-10 Ma with implied rotation rates of 15-45° Myr^{-1} (Anderson, 1971; Faulds, 1993, 1995; Faulds et al., 1994, 1995; Gans et al., 1994; Gans and Bohrson, 1998). Although it is possible to develop a more sophisticated model that inverts the data for geothermal

gradient and variable-rate rotation and exhumation, we argue that this simple analytical solution effectively interprets ZHe ages in the context of crustal rotation.

Rotated volcanic strata in the southern Highland range suggest that the footwall-rock rotation was initially rapid (~75° Myr^{-1}) for 0.5 Myr followed by slower rotation for 5.5 Myr (**Supplemental Figure 5**) (Faulds et al., 2002a,b; Hinz and Faulds, 2009). If the ca. 15.5 Ma Eldorado dikes originally intruded vertically, they suggest a rotation rate of 64-78° Myr^{-1}, including ±5° uncertainty for subvertical intrusion, from 16.2 Ma to 15.5 Ma based on their present-day ~40° east dip (**Fig. 2B**). This net rotation could also be attained via 75° Myr^{-1} for 0.5 Myr followed by 37° Myr^{-1} for 0.2 Myr. Here we test whether these kinematics could produce our observed thermochronology ages: we run a similar model as above, based on equation (3), except with rapid 75° Myr^{-1} rotation for 0.5 Myr followed by slower 15-30° Myr^{-1} rotation, assuming T_c = 180°C and dT/dz = 30°C km^{-1} (**Fig. 10**). Our data fits the modeled curves fairly well, with the exception of the anomalously older 16.4±1.3 Ma age (**Fig. 10**). Because the oldest age was from the highest paleo-position in the pluton (R=10.1 km), we speculate that the sample may have been influenced by being intruded close to, or slightly above, D_c, thus cooling faster than expected. This plot highlights that short-lived rapid early rotation does not significantly affect the ZHe ages. This is because the early rotation is least efficient at exhuming the samples toward the surface, given their circular path, and after half a million years, the samples would have only moved upwards ~1.5-3.5 km, depending on the R value, which is not enough to pass any samples through ZHe closure-temperature depth. We prefer this two-stage rotation model given that it fits the ZHe data and rotation-rate data based on rotated overlying volcanic rocks (**Fig. 10**; **Supplemental Figure 5**).

Thermal and strain history of the Searchlight pluton

Zircon U-Pb ages for Searchlight intrusions range from ca. 17 Ma to ca. 16 Ma (Bachl et al., 2001; Miller and Miller, 2002; Miller et al., 2011; Johnson, 2014) (**Fig. 11**). Zircon ages from the lower Searchlight unit are 16.6 ± 0.4 Ma, and the zircon-saturation temperatures from this unit are ~790°C (Johnson, 2014). The closure temperature of argon in hornblende is generally regarded as ~500°C (e.g., McDougall and Harrison, 1999), although fast cooling rates suggest that ~550°C may be a better estimate for the effective closure temperature of argon in hornblende in our samples (Harrison, 1982). Therefore, our argon hornblende ages spanning 17.1 Ma to 16.4 Ma are consistent with rapid cooling of the lower Searchlight >200°C over 100s kyr timespan, given the uncertainties of the applied geochronometers. This rapid cooling may have resulted from incremental piecemeal construction of the Searchlight pluton, which allowed individual intrusions to cool fairly rapidly. Specifically, the overlapping zircon and argon ages suggest that parts of the pluton cooled below ~550°C rapidly after intrusion, as has been observed in other composite plutons (Coulson et al., 2002). Assuming simple conductive cooling, a 1-2 km length-scale (L) intrusion would cool on timescales of 100-30 kyr, following $t \sim L^2/\kappa$ where κ is thermal diffusivity ($\sim 10^{-6}$ m^2 s^{-1}).

The argon thermochronology constrains that the magmatic to highest temperature sub-solidus strain occurred prior to ca. 16.4 Ma, which is the youngest age bound from our argon data (**Fig. 11**). The highest temperature fabrics (e.g., chessboard quartz extinction) and magmatic alignment of phases occurred prior to this time, which show no signs of asymmetric shearing. During the incremental assembly of the Searchlight pluton from ca. 17 Ma to ca. 16 Ma, the lower Searchlight pluton was intruded prior to the upper (**Fig. 3**), and lower Searchlight units may have been strained coaxially at magmatic state temperatures from the increasing overburden of the upper units (Faulds et al., 2001) (**Fig. 11**).

Accordingly, medium- to low-temperature sub-solidus fabrics, including quartz SGR-BLG and myrmekite and brittle fracturing in feldspars, formed after this time (**Fig. 11**). These medium- and low-temperature fabrics display eastside-up shear, suggesting that distributed shear also occurred after ca. 16.4 Ma, or after the majority of the Searchlight pluton was assembled. The youngest age constraint is provided by ZHe ages, which require these sub-solidus fabrics to have formed prior to ca. 13-14 Ma, when the pluton was cooled to ~200°C (**Fig. 11**). Combing microstructures and thermochronology, we constrain the timing of medium- to low-temperature sub-solidus fabrics to 16.4 Ma to 13-14 Ma. The majority of extension lasted from ca. 16 Ma to ca. 14 Ma (Anderson, 1971; Faulds, 1993, 1995; Faulds et al., 1994, 1995; Faulds et al., 2001, 2002a), with the most intense crustal rotation occurring prior to ca. 15 Ma (Faulds et al., 2002a; Hinz and Faulds, 2009; **Supplemental Figure 5**). Therefore, the medium- to low-temperature fabrics formed during regional extension and tilting of the Searchlight pluton (**Fig. 11**).

Models for Searchlight pluton tilting

Our above field, microstructural, and thermochronology data can constrain the tilting mechanism for the Searchlight pluton. The most significant observations to explain include: (1) 70-90° westward tilting of the Searchlight pluton, (2) two major north-striking east-directed faults bound the pluton to the west and east (i.e., the McCullough Range and Dupont Mountain faults, respectively; **Fig. 2**), and (3) north-striking intra-plutonic fabrics that predominately display eastside-up shear (**Fig. 12; Table 3**). We first outline three possible tilting models to explain these observations: (1) rigid-body rotation of the pluton via either listric or domino-style faulting, (2) antithetic imbrication approximately coeval with, or just after, either listric or domino-style faulting, or (3) flow-like rotation of the Searchlight pluton as the hot low viscosity pluton flowed toward the surface due to progressive hanging-wall

removal (**Fig. 12B; Table 3**). Next, we discuss possible processes that resulted in the observed sub-solidus shear fabrics (**Fig. 12C**).

The above three models make predictions for the broad geometries of the major normal faults and their offset magnitudes (**Table 3**). The first and second models require significant offset (>10 km) on both normal faults bounding the Searchlight pluton (**Fig. 1**) to accommodate up to 90° tilting of this pluton (**Figs. 12B; Table 3**). Tilting of the Searchlight pluton could have resulted from hanging-wall rotation in a listric normal fault system or from domino-style faulting of the McCullough and Dupont Mountain faults (panel 1 in **Fig. 12B**). For listric faulting, the McCullough Range fault would have been the listric fault responsible for tilting of the Searchlight pluton, or both the McCullough Range and Dupont Mountain faults could have been involved in domino-block tilting, which would require larger offset magnitudes than listric faulting (e.g., Wernicke and Burchfiel, 1982) (panel 1 in **Fig. 12B**). The imbrication model is similar to rigid-body rotation, except that the rotation of the Searchlight pluton is facilitated by internal antithetic faulting (panel 2 in **Fig. 12B**). The flow-like rotation model suggests that hot and relatively low viscosity footwall rocks of the Dupont Mountain fault flowed toward the surface due to progressive hanging-wall removal, isostatic uplift, and deformation of the McCullough Range fault (Spencer, 1984; Wernicke and Axen, 1988), and thus requires significant offset on the Dupont Mountain detachment fault (>10 km) but less displacement on the McCullough Range fault (≤5 km) (panel 3 in **Fig. 12B; Table 1**).

The observed intra-pluton sub-solidus fabrics may have resulted from two situations (**Fig. 12C**): (1) early pre-tilting crustal scale top-west simple shear, which would have resulted in the pervasive top-west (pre-tilting framework) sub-solidus shear observed across the pluton; or (2) sub-solidus shear during flow-like rotation model with numerous possible flow profiles, which would result in different intra-flow kinematics (e.g., predominately

eastside-up to a mix of eastside-up and eastside-down) (**Fig. 12C**). The pre-tilting shear mechanism could have resulted in subhorizontal top-west shear that was later tilted westward during rigid-body rotation or imbrication rotation (**Fig. 12**).

Each of the above models makes the following testable predictions about the relationships between intra-pluton fabrics to rotation mechanism. The rigid-body rotation models suggests the intra-plutonic contacts and fabrics were formed prior to tilting, either as magmatic or syntectonic sub-solidus fabrics developed via pre-tilting top-west simple shear (**Fig. 12C**). It is possible that minor sub-solidus strain could have occurred along the pluton margins where differential rotation caused shear between the pluton and wallrock (panel 1 of **Fig. 12B**). The imbrication model predicts eastside-up shear along spaced discrete shear zones or brittle faults (panel 2 of **Fig. 12B**). For the flow-like model, sub-solidus shear would have occurred over a range of temperatures, from magmatic temperatures to high- (500°C to >600°C) to low-sub-solidus (300-400°C) temperatures, as the footwall rocks were cooled somewhat rapidly due footwall advection (e.g., Ehlers et al., 2001; Brun et al., 2018). Although numerous flow profiles could have operated with varying predicted shear kinematics, we favor an asymmetric velocity profile because the flowing rocks would be hotter with depth, and thus the lower viscosity rocks at depth would move faster than the higher and cooler rocks. This would create a strong asymmetry to the velocity profile that would result in predominately eastside-up shear (panel 2 of **Fig. 12C**).

Although most of our fundamental observations can be reconciled with aspects of the above models, as outlined in **Table 3**, we argue that the predictions of the flow-like rotation best match observations from the tilted Searchlight pluton. We would expect the antithetic faulting in the imbrication model to have occurred relatively late during the tilting progression, and thus deformation temperatures would have been more restricted to low-temperature sub-solidus and brittle regimes. In addition, our observations of sub-solidus shear

suggest that it was relatively distributed across the pluton, and not confined to distinct shear zones as predicted for the imbrication model (panel 2 of **Fig. 12B**). For the rigid-body rotation model to explain the observed pervasive eastside-up shear fabrics there must have been pre-tilting top-west simple shear (panel 1 of **Fig. 12C**). However, the observed sub-solidus fabrics show evidence of deformation over a range of high to low temperatures with consistent kinematics (**Fig. 11**), which suggests this deformation occurred while the rocks were cooling, and possibly moving toward the surface. Pre-tilting simple shear would be expected to occur over more limited temperature ranges, as commonly observed in exhumed detachment faults (e.g., Behr and Platt, 2011; Gébelin et al., 2015). There also a very narrow time window, within uncertainties, between final pluton emplacement (by 16.2 Ma) and crustal tilting (starting at ca. 16.2 Ma) for the top-west simple shear to have occurred, especially when considering the Dupont-Mountain-fault activity involved top-east shear. Although possible, this is harder to reconcile.

Three primary lines of evidence corroborate our flow-like rotation model. First, our observations of mostly eastside-up sub-solidus shear across most of our pluton, over a range of inferred temperatures, is consistent with the flow-like rotation model. Sub-solidus strain is most evident in the middle-to-lower parts of the pluton, but observations of north-striking fabrics across the entire pluton display a range of predominately eastside-up to ambiguous shear fabrics (**Fig. 6**). Second, there are other indications that suggest that the bulk of the pluton sheared upward to the east relative to the surrounding country rock, including observations of a kilometer-scale *a*-type fold (**Fig. 5**) and the negative correlation between ZHe ages and distance away from the northern pluton-wallrock margin (**Supplemental Figure 2B**). This thermochronology data suggests that the samples toward the middle of the pluton moved faster toward the surface than those near the margins, and thus were exhumed from greater depths, consistent with a flow-like model. Simple conductive cooling of the

pluton would have the center of the pluton cooling slower than its margins, which would have resulted in younger ZHe ages in the pluton's center and older ages along its margins.

Third, east-directed offset on the McCullough Range fault in the central Highland Range, west of the southern Highland Range (**Fig. 2**), is approximately 5 km based on the anticline geometry and minimum offset required to restore the base of the Cenozoic volcanic rocks (Faulds et al., 2002a,b). This offset magnitude is not enough to tilt the >15-km-wide hanging-wall rocks of this normal fault to the east 90° west, as required for the rigid-body rotation and imbrication models (**Figs. 12B and C**).

In summary, based on our observations outlined in this study, we suggest that the Searchlight pluton rotated 90° on its side via a flow-like mechanism (**Fig. 12C**). The relative velocity field of this flow up toward the surface to the east would result in predominately eastside-up shear, and occasional ambiguous shear may have resulted from local minimal differences in the relative flow velocities. We emphasize that pre-tilting top-west simple shear followed by relatively rigid-body rotation is permissible, but available observations better support the flow-like rotation model.

This tilting mechanism may apply to other pluton-dominated footwall rocks in the Colorado River Extensional Corridor, including the Aztec Wash and Spirit Mountain plutons (**Fig. 1**). Both of these regions involve a similar intrusion and extension history, although at differing scales and orientations (e.g., Faulkner et al., 1995; Walker et al., 2007). Future study of these regions will provide valuable tests to our model outlined above.

Tectonic model

Here we outline a tectonic model focusing on the tilting of the Searchlight pluton in the footwall of the Dupont Mountain fault (**Fig. 13**). First, we note that 90° restoration of the

Searchlight pluton and adjacent country wallrock, including the Ireteba pluton, restores the Ireteba pluton's previously mapped BDT, constrained by sub-solidus fabrics (Faulds et al., 2001; Hinz et al., 2012a, 2012b), to pre-Searchlight-tilting paleodepths of ~12-14 km (**Fig. 2**). This BDT transition was previously assumed to be Miocene in age because parallel fabrics crosscut and distort Miocene dikes and the Miocene Searchlight-Ireteba contact (**Fig. 2**).The Cretaceous Ireteba pluton would have been at steady-state crustal temperatures prior to Miocene plutonism and extension, and therefore the Ireteba BDZ location predicts that the Miocene geothermal gradient outside of the Searchlight intrusion was 300-350°C divided by 12-14 km, or approximately 21-29°C km^{-1}.

By ca. 16.2 Ma, we assume that a ~10 km by ~10 km rectangle (cross-section view; **Fig. 13B**) Searchlight plutonic complex was fully emplaced, which consisted of different aged intrusions and dikes that started intruding at ca. 17 Ma as described above (**Fig. 13B**) (e.g., Bachl et al., 2001; Miller and Miller, 2002; Miller et al., 2011; Johnson, 2014). The overlying volcanic rocks are genetically related to the Searchlight intrusions, and the basal rocks were erupted during this 17-16 Ma interval. The amalgamated Searchlight plutonic system is hotter than background temperatures, with a background geothermal gradient of ~25°C km^{-1} as discussed above (Hinz et al., 2012a, b). Elevated crustal temperatures may have weakened the upper crust locally, facilitating rapid extension (Gans et al., 1989).

Starting at ca. 16.2 Ma, rapid east-west extension initiates, and both the McCullough Range and Dupont Mountain faults actively accommodate east-directed motion (**Fig. 13C**). A ~10-km-wavelength north-trending anticline develops in the hanging wall of the McCullough Range fault during this extension (Faulds et al., 2002a). The removal of the Dupont Mountain hanging wall and its associated overburden caused the footwall rocks to flow toward the surface due to pressure gradient (i.e., Poiseuille flow). This flow was concentrated in a channel originally defined by the dimensions of the

Searchlight pluton because this would have been hot and less viscous than the surrounding country rock. The country rock around the Searchlight pluton at depths equivalent to the paleo-base depth of the pluton prior to tilting (i.e., ~10-13 km depth) would have been 250-325°C based on the background geothermal gradient. Immediately after intrusion, the Searchlight pluton would have been at least 250-350°C hotter. Assuming wet quartzite power-law rheology, an increase of ~300°C equates to an order-of-magnitude reduction in effective viscosities (Gleason and Tullis, 1995; Hirth et al., 2001). This viscosity disparity would allow the pluton footwall to flow because of a pressure gradient resulting from the removal of the hanging-wall rocks (**Fig. 13D**). At ca. 15.5 Ma, Eldorado dike swarm rocks intruded the rotating system vertically, and their present-day orientation dipping ~45° east (**Fig. 2B**) indicates that the Searchlight pluton had rotated ~45° by this time (**Fig. 13D**). During crustal tilting volcanism continued and resulted in tilt fanning observed in the volcanic section (Faulds et al., 2002a,b)

The discrepancy between the 90° tilted overlying volcanic rocks and the predominance of fabrics dipping 60-70°W may be related to the flow-like rotation mechanism. The colder and more rigid roof and walls of the pluton may have rotated at a different rate than the hotter and weaker flowing pluton. Alternatively, fossilized flow patterns just below the surface would have been less steep than those at the surface, and therefore subsequent erosion may have exposed the less-than-vertical fabrics. Elevations decrease to the east, toward the Colorado River (**Fig. 1**), and therefore the eastern map area exposes slightly deeper structural levels with potentially more gently dipping fabrics.

In our model, the Dupont Mountain fault initiates as a steep fault, as fault-cutoff relationships suggest (Ruppert and Faulds, 1999; Faulds et al., 2002a). These orientations are mechanically more favorable than postulated low-angle (e.g., <30°) normal faulting. We envision the faults becoming subhorizontal at ~15 km depth, which may generally

correspond to a weak layer in the middle crust that may exist below the brittle-ductile transition (Cooper et al., 2010; Platt et al., 2015). Although speculative, this aspect of our model appears geometrically plausible based on current knowledge.

The steep formation angle and location of the Dupont Mountain fault may indicate that the fault formed along Searchlight pluton's eastern margin (**Figs. 2** and **13**). This position may be controlled by strength contrasts between the hotter and weaker pluton and the colder and stronger country rock, and in this sense, the Dupont Mountain detachment fault is similar to oceanic core complexes (e.g., Ildefonsee et al., 2007; Lagabrielle et al., 2015). Tucholke et al. (2008) explored how the volume of preceding melt emplacement strongly controls detachment faulting in oceanic core complexes (e.g., Olive et al., 2010). Similarly, the Searchlight pluton predates Dupont Mountain faulting, and this comparison to oceanic core complexes may serve as a useful analog. Large pre-extensional intrusions across the Basin and Range, with their associated thermal perturbations, probably affected the kinematics and geometry of crustal extension (Gans et al., 1989). That said, preceding magmatism is clearly not a requirement for all continental detachment fault systems (e.g., Platt et al., 2015), and just north of Lake Mead similar-aged detachment faults in the Mormon-Beaver Dam Mountains do not involve preceding intrusions (e.g., Bidgoli et al., 2015).

Kinematic cooling model

Whether extension involves primarily pure- or simple-shear affects the thermal history of the crust (e.g., McKenzie, 1978; Wernicke, 1985; Buck, 1988, 1991) (**Fig. 14**). Simple-shear extension facilitated by footwall rotation, as exemplified here, involves significant footwall advection that may more efficiently cool the crust than a pure-shear extensional mechanism (**Fig. 14**). We explore this hypothesis via simple scaling analysis to constrain the cooling effects of rock advection (e.g., Cao et al., 2019). We use the following

2D kinematic framework (**Fig. 15**). The footwall rotates about a surface pivot (z=0) along an initially vertical arm, with length D. The pluton-arm rotates counterclockwise with an angular velocity ω, such that the angle between the rotation arm and the surface (α) decreases with time. The vertical velocity v_z (i.e., negative z direction; **Fig. 15**) of a point along the rotation arm varies as a function of α, D, and ω (radians/second):

$$v_z(D, \omega, \alpha) = D\omega \cos \alpha \quad (8)$$

We assume that v_z motion is effectively balanced in z direction by erosion and/or extensional thinning. Because we are interested in the upward motion of the rock from depth toward the Earth's surface, the rock-advection parameter is simplified to $V = |v_z|$.

The ratio of conductive to advective cooling time is quantified by the Péclet number Pe:

$$Pe = \frac{VL}{\kappa} \quad (9)$$

where V is vertical motion of the rock balanced by surface erosion and tectonic vertical thinning, L is the characteristic length scale of the system of interest, and κ is thermal diffusivity. For $Pe > 1$, advective cooling dominates whereas smaller values, especially $Pe \ll 1$, demonstrate the importance of conductive cooling. McKenzie (1978)'s original pure-shear extension model was based on one-dimensional conductive cooling of the crust after instantaneous extension; thus, the characteristic cooling time $t \sim L^2/\kappa$ (**Fig. 14**). This assumes no mass or heat advection (i.e., $Pe \approx 0$) after the instantaneous extension, which is a reasonable approximation compared to simple-shear extension (e.g., Wernicke, 1981; Spencer, 1984; **Fig. 14**). Pure-shear extension classically involves slower advection of the footwall rocks compared to simple-shear-driven footwall exhumation from mid-crustal depths (Spencer, 1984; Brun et al., 1994; Wernicke and Axen, 1988; Gessner et al., 2007; Rey et al., 2009), as exemplified by 90° Searchlight-pluton rotation in the Dupont Mountain detachment system. Thus, $Pe > 0$, and incorporating advection into the conductive cooling model of the crust results in:

$$t \sim \frac{L^2}{\kappa\,(1+\mathrm{Pe})} \tag{10}$$

Combining equations (9) and (10) yields

$$t \sim \frac{L}{\left(\frac{\kappa}{L}+V\right)} \tag{11}$$

Our goal here is to provide order-of-magnitude estimates for crustal cooling that can be generally applied to all extensional systems. The estimates below assume only conduction and advection with a constant diffusivity value, although convection and hydrothermally affected or temperature-dependent diffusivity will affect cooling times (e.g., Norton, 1979; Taylor, 1990; Nabelek et al., 2012; Gelman et al., 2013; Cao et al., 2019). For example, a ~600°C temperature drop can yield a nearly fourfold increase in thermal diffusivity (Whittington et al., 2009; Nabelek et al., 2012).

For the Searchlight pluton we assume that footwall rotation is either fast, ω = 75° Myr^{-1} (2.4×10^{-12} ° s^{-1}) or slow, ω = 15° Myr^{-1} (i.e., 4.8×10^{-13} ° s^{-1}) (**Fig. 16A**). Near the base of the pluton, D equals ~13 km, and V ranges from 0 km Myr^{-1} to 3.4 km Myr^{-1} (ω=15° Myr^{-1}) and 0 km Myr^{-1} to 17 km Myr^{-1} (ω=75° Myr^{-1}) depending on $\alpha(t)$ (**Fig. 16A**). These values yield *Pe* numbers ranging from 0 to ~5.5 (**Fig. 16A**). For a slow rotation rate, advection is insignificant (*Pe*<<1). For rapid rotation, *Pe* surpasses a value of 1 rather quickly, in ~10° rotation or ~0.13 Myr.

Assuming L=10km (i.e., the approximate length and width of the Searchlight pluton), simple conductive cooling suggests that the pluton should cool to background steady-state temperatures in 3.2 Myr, assuming a constant thermal diffusivity of 10^{-6} m^2 s^{-1} (**Fig. 16B**). Halving thermal diffusivity (5^{-7} m^2 s^{-1}) doubles the cooling time, 6.3 Myr (**Fig. 16B**), especially considering diffusivity decreases with increasing temperature. The vertical rock motion required by our kinematic model (**Figs. 16**) modifies a simple conductive cooling scenario ($t \sim L^2/\kappa$), as in equation (11). Incorporation of V leads to characteristic cooling

times that are significantly shorter than simple conductive cooling (**Fig. 16B**). The actual difference depends on the assumed rotation rate and time because modeled V varies as a function of α.

To compare the two cooling models, we note when the model curves intersect a line of slope 1 on **Figure 16B**. This time is when the modeled tilting duration equals the characteristic cooling time, and thus the heated crust of length scale L should have cooled back to steady-state temperatures. A shorter time intersection suggests a faster cooling rate. Including vertical advection following the rotational kinematics leads to cooling times that are ~1/3 and ~2/3 that of simple conductive cooling, given fast (75° Myr^{-1}) and slow (15° Myr^{-1}) rotation rates respectively. With a lower diffusivity value, this difference is even greater: ~6 Myr intersection for conductive cooling, ~2.5 Myr intersection for slow rotation, and ~1.5 Myr intersection for fast rotation (**Fig. 16B**).

This scaling analysis shows that footwall rotation and vertical rock advection is more efficient at cooling the crust than conduction alone. The differences are likely even greater given the fact diffusivity is inversely temperature dependent (Whittington et al., 2009; Nabelek et al., 2012). All things being equal, fast cooling may increase thermal diffusivity and further reduce the characteristic cooling time (**Fig. 16B**). Therefore, fast cooling via vertical advection is a positive feedback: rapid cooling spurred by significant advection will result in an increase in thermal diffusivity, which will result in net faster cooling.

A final consideration is that the fast rotation curve (75° Myr^{-1}) intersects the line of slope 1 in ~1 Myr, which broadly correlates with the timing of initial fast rotation derived from tilted volcanic strata and dikes (**Supplementary Figure 5**). We hypothesize that the initial rapid cooling may have rapidly cooled the crust, as our cooling analysis shows, driving a slowdown of extension and rotation rates.

Crustal cooling and the strength of the crust

Frictional sliding of the upper brittle crust is pressure-dependent and the crust gets stronger with depth (Brace and Kohlstedt, 1980). When crustal temperatures are high enough to thermally activate viscous flow, crustal strength becomes inversely dependent on temperature following an Arrhenius relationship. An increase in temperature corresponds to a rapid decrease in strength, proportional to $e^{\frac{1}{T}}$. Accordingly, the geothermal gradient of the crust controls the location of the brittle-ductile transition, and if crustal strength resides predominately in the brittle crust (Lister and Davis, 1989; Jackson et al., 2008; Zuza et al., 2017; Zuza and Carlson, 2018), the depth of brittle-ductile transition is proportional to the yield strength of the crust.

The intrusion of the relatively hot Searchlight pluton would have weakened the crust locally by raising the geothermal gradient and reducing the brittle-crust thickness. For example, doubling the geothermal gradient is expected to reduce the effective yield strength of the crust by more than a factor of two. This may have led to rapid extension and footwall tilting following the emplacement of the 17-16 Ma pluton. Footwall-advection dominated extension, as outlined in this study, rapidly cooled the crust, which would have quickly re-strengthened the crust. Halving the thermal gradient would lead to an approximate twofold increase in brittle-crust strength. We envision that the process of rapid extension, possibly promoted by voluminous magmatism, acts as a negative feedback: (1) fast extension (~10^{-14} s^{-1}) drives rapid advection of hotter deeper rocks through a simple shear process such as footwall rotation, (2) vertical footwall advection results in more efficient and effective crustal cooling, and (3) rapidly cooling the crust quickly strengthens it, which (4) leads to the cessation of rapid extension. This slowdown in extensional rate in the Colorado extensional

corridor is evidenced by lower-magnitude offset high-angle normal fault activity following the phase of rapid detachment faulting (e.g., Faulds et al., 2001).

There are two possible alternative explanations for short-duration fast extension. One is that the locations of rapid extension correlated with regions of previously thickened crust, and therefore gravitational potential energy may drive rapid extension (e.g., Molnar and Lyon-Caen, 1988; England and Molnar, 1997). Accordingly, the subsequent thinning of the crust reduces this potential energy and slows extension. Second, changes in plate-boundary conditions also affected the temporal and spatial distribution of deformation and strain rates across the CREC (Faulds and Henry, 2008). The initiation of the dextral Walker Lane and Las Vegas Valley shear zones is coincident with the ultimate termination of CREC extension (Gans and Bohrson, 1998; Faulds et al., 2001), which highlights how the reorganization of intracontinental strain partitioning along the Pacific-North American plate boundary impacted CREC evolution.

Our proposed feedback specifically relates to fault systems where the crust was heated prior to deformation and crustal advection. Classically, crustal thinning of steady-state crust is thought to compress crustal isotherms, increase thermal gradients, and thin and weaken the brittle crust (e.g., Ketcham, 1996; Rey et al., 2009). For the Searchlight case, we envision a dynamic crustal cooling rate where fast strain rates and advection of the hot thermal anomaly toward the surface in a simple-shear fashion is faster than advection of middle-lower crustal rocks via a pure-shear thinning process.

The process outlined here may be applicable to other extensional systems across the western US and globally, although it is most applicable to systems that involve voluminous intrusions prior to extension. For example, in Yerington, NV, and Vulture Mountains, AZ, voluminous and widespread volcanism was followed by one to several million years of rapid extension (10^{-14} s^{-1}) (e.g., Proffett, 1977; Dilles and Gans, 1995; Spencer et al., 1995). It has

previously been proposed that rapid extension suppresses local volcanism (Gans and Bohrson, 1998), and we envision that rapid advection hot crust may be an additionally important process for effectively cooling the crust, thus slowing extensional rates. Across the Basin and Range of the western US, high-magnitude extension with significant footwall advection is followed by high-angle normal faulting with comparatively lower offsets (e.g., Profett, 1977; Gans and Miller, 1983; Snoke et al., 1997; Gans and Bohrson, 1998).

Conclusions

In this study we provide field, microstructural, EBSD, and thermochronological observations from across the Miocene Searchlight pluton to investigate the mechanism of 90° horizontal-axis tilting of this pluton. Specifically, we tested models of rigid-body rotation, footwall imbrication, and flow-like rotation of the Searchlight pluton. Our observations show that much of the Searchlight pluton experienced protracted deformation over a range of temperatures, from magmatic state to sub-solidus, with pervasive eastside-up shear. Near the pluton margins, flow of the pluton upward relative to the country rock is observed as a 1 km-scale *a*-type fold. These observations are most consistent with the flow-like rotation model in which hotter and lower viscosity footwall of the Dupont Mountain fault, consisting of the Searchlight pluton, flowed upwards toward the surface during removal of the overburden hanging-wall rocks. The fault's initial location may have been controlled by the eastern pluton margin, due to strength contrasts between the weaker intrusion and stronger country rock, which is analogous to oceanic core complexes.

The pluton intruded incrementally from 17 Ma to 16 Ma, with each intrusion cooling rapidly as observed from overlapping U-Pb zircon and $^{40}Ar/^{39}Ar$ hornblende ages. Our bulk zircon helium thermochronology demonstrates that the Searchlight pluton cooled below ~200°C by 14-13 Ma. The ZHe cooling ages are younger in the east than the west,

which is consistent with faster cooling of the eastern samples relative to the western samples following horizontal-axis rotation of the Searchlight pluton. Simple kinematic models of this rotation corroborate other constraints from tilted volcanic strata and cross-cutting dikes that suggest initial rapid rotation (~75° Myr^{-1}) at 16.2-15.7 Ma followed by more modest exhumation rates until ca. 13 Ma.

First-order scaling analyses highlight how advection by flow-like rotation more effectively cools the upper crust than pure-shear extension with conductive cooling. The fast cooling associated with this rotation process results in a negative feedback whereby the rapidly cooled crust becomes strong enough to halt further simple-shear style extension. This feedback may explain why rapid extension was short lived and further extension is mostly accommodated by high-angle normal faults with significantly lower offsets that developed in a colder and stronger crust.

Acknowledgments

This research was support by the Tectonics Program of the National Science Foundation (EAR 1830139), startup funds, and a New Scholarly Endeavour grant at UNR (Zuza and Cao). Discussion in the field with Calvin Miller, Mike Eddy, Blair Schoene, and Ayla Pamukcu are greatly appreciated. We thank Jon Spencer, Gary Axen, and an anonymous reviewer for thorough reviews, and detailed comments by Associate Editor Ernst Willingshofer, that together greatly improved the clarity and presentation our ideas in this manuscript. All data supporting the interpretations and conclusions of this study can be found in 1:24,000-scale geologic maps published by the Nevada Bureau of Mines and Geology, the manuscript text, Table 2, the supporting information file, and specifically Supporting Tables 2 and 3 in the supporting information file. There are no restrictions to this data usage.

References

Allmendinger, R. W., Sharp, J. W., Von Tish, D., Serpa, L., Brown, L., Kaufman, S., Oliver, J., & Smith, R. B. (1983). Cenozoic and Mesozoic structure of the eastern Basin and Range province, Utah, from COCORP seismic-reflection data. *Geology*, *11*(9), 532-536.

Anderson, R. E. (1971). Thin skin distension in Tertiary rocks of southeastern Nevada. *Geological Society of America Bulletin*, *82*(1), 43-58.

Anderson, J. L., & Smith, D. R. (1995). The effects of temperature and f O2 on the Al-in-hornblende barometer. *American Mineralogist, 80*, 549.

Armstrong, P. A., Taylor, A. R., & Ehlers, T. A. (2004). Is the Wasatch fault footwall (Utah, United States) segmented over million-year time scales?. *Geology*, *32*(5), 385-388.

Axen, G. J., Grove, M., Stockli, D., Lovera, O. M., Rothstein, D. A., Fletcher, J. M., Farley, K., & Abbott, P. L. (2000). Thermal evolution of Monte Blanco dome: Low-angle normal faulting during Gulf of California rifting and late Eocene denudation of the eastern Peninsular Ranges. *Tectonics*, *19*(2), 197-212.

Axen, G. J., Taylor, W. J., & Bartley, J. M. (1993). Space-time patterns and tectonic controls of Tertiary extension and magmatism in the Great Basin of the western United States. *Geological Society of America Bulletin, 105*(1), 56-76.

Bachl, C. A., Miller, C. F., Miller, J. S., & Faulds, J. E. (2001). Construction of a pluton: Evidence from an exposed cross section of the Searchlight pluton, Eldorado Mountains, Nevada. *Geological Society of America Bulletin*, *113*(9), 1213-1228.

Bachmann, F., Hielscher, R., Jupp, P. E., Pantleon, W., Schaeben, H., & Wegert, E. (2010). Inferential statistics of electron backscatter diffraction data from within individual crystalline grains. *Journal of Applied Crystallography*, *43*(6), 1338-1355.

Beaumont, C., Jamieson, R. A., Nguyen, M. H., & Lee, B. (2001). Himalayan tectonics explained by extrusion of a low-viscosity crustal channel coupled to focused surface denudation. *Nature*, *414*(6865), 738-742.

Behr, W. M., & Platt, J. P. (2011). A naturally constrained stress profile through the middle crust in an extensional terrane. Earth and Planetary Science Letters, 303(3-4), 181-192.

Best, M. G., Christiansen, E. H., de Silva, S., & Lipman, P. W. (2016). Slab-rollback ignimbrite flareups in the southern Great Basin and other Cenozoic American arcs: A distinct style of arc volcanism. *Geosphere, 12*(4), 1097-1135.

Bidgoli, T. S., Stockli, D. F., & Walker, J. D. (2015). Low-temperature thermochronologic constraints on the kinematic histories of the Castle Cliffs, Tule Springs, and Mormon Peak detachments, southwestern Utah and southeastern Nevada. *Geosphere*, *11*(3), 850-867.

Blumenfeld, P., & Bouchez, J. L. (1988). Shear criteria in granite and migmatite deformed in the magmatic and solid states. *Journal of Structural Geology, 10*(4), 361-372.

Blumenfeld, P., Mainprice, D., & Bouchez, J. L. (1986). C-slip in quartz from subsolidus deformed granite. *Tectonophysics, 127*(1-2), 97-115.

Brace, W. F., & Kohlstedt, D. L. (1980). Limits on lithospheric stress imposed by laboratory experiments. *Journal of Geophysical Research: Solid Earth, 85*, 6248-6252.

Braun, J., Stippich, C., & Glasmacher, U. A. (2016). The effect of variability in rock thermal conductivity on exhumation rate estimates from thermochronological data. *Tectonophysics, 690*, 288-297.

Brun, J. P., Sokoutis, D., Tirel, C., Gueydan, F., Van den Driessche, J., & Beslier, M. O. (2018). Crustal versus mantle core complexes. *Tectonophysics*, 746, 22-45.

Brun, J. P., Sokoutis, D., & Van Den Driessche, J. (1994). Analogue modeling of detachment fault systems and core complexes. *Geology, 22*(4), 319-322.

Buck, W. R., Martinez, F., Steckler, M. S., & Cochran, J. R. (1988). Thermal consequences of lithospheric extension: pure and simple. *Tectonics*, *7*(2), 213-234.

Buck, W. R. (1988). Flexural rotation of normal faults. *Tectonics*, *7*(5), 959-973.

Buck, W. R. (1991). Modes of continental lithospheric extension. *Journal of Geophysical Research: Solid Earth*, *96*(B12), 20161-20178.

Cao, W., Paterson, S., Saleeby, J., & Zalunardo, S. (2016). Bulk arc strain, crustal thickening, magma emplacement, and mass balances in the Mesozoic Sierra Nevada arc. *Journal of Structural Geology*, *84*, 14-30.

Cao, W., Lee, C. T. A., Yang, J., & Zuza, A. V. (2019). Hydrothermal circulation cools continental crust under exhumation. *Earth and Planetary Science Letters, 515*, 248-259.

Carreras, J., Druguet, E., & Griera, A. (2005). Shear zone-related folds. *Journal of Structural Geology, 27*(7), 1229-1251.

Cates, N.L., Miller, J.S., Miller, C.F., Wooden, J.L., Eriksen, S., & Means, M. (2003) *Longevity of plutonic systems: SHRIMP evidence from Aztec Wash and Searchlight plutons, Nevada.* Abstract presented at the Geological Society of America conference.

Cobbold, P. R., & Quinquis, H. (1980). Development of sheath folds in shear regimes. *Journal of Structural Geology, 2*(1-2), 119-126.

Cole, D. R., Horita, J., Polyakov, V. B., Valley, J. W., Spicuzza, M. J., & Coffey, D. W. (2004). An experimental and theoretical determination of oxygen isotope fractionation in the system magnetite-H_2O from 300 to 800 C. *Geochimica et Cosmochimica Acta*, *68*(17), 3569-3585.

Cole, E. D. (1989). *Pedogenesis of late Cenozoic alkalic basalt near the eastern boundary of the Basin-and-Range: Upper Grand Wash trough, Arizona and Gold Butte, Nevada* (Master's thesis). Las Vegas, Nevada, University of Nevada.

Colleps, C. L., McKenzie, N. R., Stockli, D. F., Hughes, N. C., Singh, B. P., Webb, A. A. G., Myrow, P. M., Planavsky, N. J., & Horton, B. K. (2018). Zircon (U- Th)/He Thermochronometric Constraints on Himalayan Thrust Belt Exhumation, Bedrock Weathering, and Cenozoic Seawater Chemistry. *Geochemistry, Geophysics, Geosystems*, *19*(1), 257-271.

Cooper, F. J., Platt, J. P., Anczkiewicz, R., & Whitehouse, M. J. (2010). Footwall dip of a core complex detachment fault: Thermobarometric constraints from the northern Snake Range (Basin and Range, USA). *Journal of Metamorphic Geology*, *28*(9), 997-1020.

Coulson, I. M., Villeneuve, M. E., Dipple, G. M., Duncan, R. A., Russell, J. K., & Mortensen, J. K. (2002). Time-scales of assembly and thermal history of a composite felsic

pluton: constraints from the Emerald Lake area, northern Canadian Cordillera, Yukon. *Journal of Volcanology and Geothermal Research*, 114(3-4), 331-356.

Cross, A. J., & Skemer, P. (2017). Ultramylonite generation via phase mixing in high- strain experiments. *Journal of Geophysical Research: Solid Earth*, *122*(3), 1744-1759.

Cross, A. J., Prior, D. J., Stipp, M., & Kidder, S. (2017). The recrystallized grain size piezometer for quartz: An EBSD-based calibration. *Geophysical Research Letters, 44*(13), 6667-6674.

Chapman, A. D., Kidder, S., Saleeby, J. B., & Ducea, M. N. (2010). Role of extrusion of the Rand and Sierra de Salinas schists in Late Cretaceous extension and rotation of the southern Sierra Nevada and vicinity. *Tectonics, 29*(5).

Christiansen, R. L., and Yeats, R. S. (1992). Post Laramide geology of the U.S. Cordilleran region. In B. C. Burchfiel, P. W. Lipman, M. L. Zoback (Eds*.), The Cordilleran orogen: conterminous U.S.* (Vol. G-3, pp. 261-406). Boulder, CO: Geological Society of America.

DeCelles, P. G., Ducea, M. N., Kapp, P., & Zandt, G. (2009). Cyclicity in Cordilleran orogenic systems. *Nature Geoscience*, *2*(4), 251-257.

de Araújo, M. N. C., da Silva, F. C. A., de Sá, E. F. J., Holcombe, R. J., & de Vasconcelos, P. M. (2003). Microstructural evolution of the Serido Belt, NE-Brazil: the effect of two tectonic events on development of c-axis preferred orientation in quartz. *Journal of Structural Geology*, 25(12), 2089-2107.

Dilles, J. H., & Gans, P. B. (1995). The chronology of Cenozoic volcanism and deformation in the Yerington area, western Basin and Range and Walker Lane. *Geological Society of America Bulletin*, *107*(4), 474-486.

Dimanov, A., & Dresen, G. (2005). Rheology of synthetic anorthite-diopside aggregates: Implications for ductile shear zones. *Journal of Geophysical Research: Solid Earth*, *110*(B7).

Dodge, M.C., Miller, J.S., Faulds, J.E., & Miller, C.F. (2005). *An erupted record from the Miocene Searchlight pluton, Nevada*. Abstract presented at the Geological Society of America Conference.

Ehlers, T. A., Armstrong, P. A., & Chapman, D. S. (2001). Normal fault thermal regimes and the interpretation of low-temperature thermochronometers. *Physics of the Earth and Planetary Interiors*, 126(3-4), 179-194.

Ehlers, T. A., Willett, S. D., Armstrong, P. A., & Chapman, D. S. (2003). Exhumation of the central Wasatch Mountains, Utah: 2. Thermokinematic model of exhumation, erosion, and thermochronometer interpretation. *Journal of Geophysical Research: Solid Earth*, *108*(B3).

England, P., & Molnar, P. (1997). Active deformation of Asia: From kinematics to dynamics. *Science*, *278*(5338), 647-650.

Falkner, C. M., Miller, C. F., Wooden, J. L., & Heizler, M. T. (1995). Petrogenesis and tectonic significance of the calc-alkaline, bimodal Aztec Wash pluton, Eldorado Mountains, Colorado River extensional corridor. *Journal of Geophysical Research*, *B100*, p. 10453–10476.

Faulds, J. E. (1995). *Geologic map of the Mt. Davis 7.' quadrangle, Nevada and Arizona*. Nevada Bureau of Mines and Geology (Map 105, scale 1:24 000).

Faulds, J. E. (1993). Miocene stratigraphy of the central Black Mountains, northwestern Arizona: Variations across a major accommodation zone. *Tertiary stratigraphy of highly extended terranes, California, Arizona, and Nevada: US Geological Survey Bulletin*, *2053*, 37-44.

Faulds, J. E., Olson, E. L., Harlan, S. S., & McIntosh, W. C. (2002a). Miocene extension and fault-related folding in the Highland Range, southern Nevada: A three-dimensional perspective. *Journal of Structural Geology, 24*(4), 861-886.

Faulds, J. E., Bell, J. W., Olson, E. L., & Chaney, R. L. (2002b). *Geologic map of the Nelson SW Quadrangle, Clark County, Nevada*. Nevada Bureau of Mines and Geology (Map 134, scale 1:24,000).

Faulds, J. E., Ramelli, A. R., & Castor, S. B. (2010*). Preliminary geologic map of the Searchlight quadrangle, Clark County, Nevada.* Nevada Bureau of Mines and Geology (scale 1:24,000).

Faulds, J. E., Geissman, J. W., & Mawer, C. K. (1990). Structural development of a major extensional accommodation zone in the Basin and Range province, northwestern Arizona and southern Nevada: Implications for kinematic models of continental extension. *Geological Society of America Memoir, 176*, p. 37-76.

Faulds, J. E., Feuerbach, D. L., Miller, C. F., & Smith, E. I. (2001). Cenozoic evolution of the northern Colorado River extensional corridor, southern Nevada and northwest Arizona. *Pacific Section of the American Association of Petroleum Geologists Publication, 78*, p. 239-272.

Faulds, J. E., Gans, P. B., & Smith, E. I. (1994). *Spatial and temporal patterns of extension in the northern Colorado River extensional corridor, northwestern Arizona and southern Nevada*. Abstract presented at the Geological Society of America conference.

Faulds, J. E., Feuerbach, D. L., Reagan, M. K., Metcalf, R. V., Gans, P., and Walker, J. D. (1995). The Mt. Perkins block, northwestern Arizona: An exposed cross section of an evolving, preextensional to synextensional magmatic system. *Journal of Geophysical Research*, 100, 15249-15266.

Faulds, J. E., Shaw, M., & Miller, C. F. (1996). *Progressive development of metamorphic core complexes and detachment faults, Colorado River extensional corridor, western USA.* Abstract presented at the Geological Society of America conference.

Faulds, J. E., Feuerbach, D. L., Miller, C. F., & Smith, E. I. (2001). Cenozoic evolution of the northern Colorado River extensional corridor, southern Nevada and northwest Arizona. *Pacific Section of the American Association of Petroleum Geologists Publication, 78*, p. 239-272.

Faulds, J. E. & Henry, C. D. (2008). Tectonic influences on the spatial and temporal evolution of the Walker Lane: An incipient transform fault along the evolving Pacific–North American plate boundary. *Ores and orogenesis: Circum-Pacific tectonics, geologic evolution, and ore deposits: Arizona Geological Society Digest, 22,* 437-470.

Ferguson, C. A., McIntosh, W. C., & Miller, C. F. (2013). Silver Creek caldera—The tectonically dismembered source of the Peach Spring Tuff. *Geology*, *41*(1), 3-6.

Feuerbach, D. L., Smith, E. I., Walker, J. D., & Tangeman, J. A. (1993). The role of the mantle during crustal extension: Constraints from geochemistry of volcanic rocks in

the Lake Mead area, Nevada and Arizona. *Geological Society of America Bulletin*, *105*(12), 1561-1575.

Gans, P. B., & Bohrson, W. A. (1998). Suppression of volcanism during rapid extension in the Basin and Range Province, United States. *Science*, *279*(5347), 66-68.

Gans, P. B., Mahood, G. A., & Schermer, E. R. (1989), Synextensional magmatism in the Basin and Range province: A case study from the eastern Great Basin. *Geological Society of America Special Paper, 233*, 1-53.

Gans, P. B., & Miller, E. L. (1983). Style of mid-Tertiary extension in east-central Nevada. *Geological excursions in the overthrust belt and metamorphic core complexes of the Intermountain region: Utah Geological and Mineral Survey Special Studies*, 59, 107-139.

Gans, P. B., Landau, B., and Darvall, P. (1994). *Ashes, ashes, all fall down: Caldera-forming eruptions and extensional collapse of the Eldorado Mountains, southern Nevada.* Abstract presented at the Geological Society of America conference.

Gébelin, A., Teyssier, C., Heizler, M. T., & Mulch, A. (2015). Meteoric water circulation in a rolling-hinge detachment system (northern Snake Range core complex, Nevada). *GSA Bulletin, 127*(1-2), 149-161.

Gelman, S. E., Gutiérrez, F. J., & Bachmann, O. (2013). On the longevity of large upper crustal silicic magma reservoirs. *Geology, 41*(7), 759-762.

Gessner, K., Wijns, C., & Moresi, L. (2007). Significance of strain localization in the lower crust for structural evolution and thermal history of metamorphic core complexes. *Tectonics*, *26*(2).

Glazner, A. F., Nielson, J. E., Howard, K. A., & Miller, D. M. (1986). Correlation of the Peach Springs Tuff, a large-volume Miocene ignimbrite sheet in California and Arizona. *Geology*, *14*(10), 840-843.

Glazner, A. F., & Bartley, J. M. (1984). Timing and tectonic setting of Tertiary low-angle normal faulting and associated magmatism in the southwestern United States. *Tectonics, 3*(3), 385-396.

Gleason, G. C., & Tullis, J. (1995). A flow law for dislocation creep of quartz aggregates determined with the molten salt cell. *Tectonophysics*, *247*(1-4), 1-23.

Goetze, C., & Evans, B. (1979). Stress and temperature in the bending lithosphere as constrained by experimental rock mechanics. *Geophysical Journal International*, *59*(3), 463-478.

Guenthner, W. R., Reiners, P. W., Ketcham, R. A., Nasdala, L., & Giester, G. (2013). Helium diffusion in natural zircon: Radiation damage, anisotropy, and the interpretation of zircon (U-Th)/He thermochronology. *American Journal of Science*, *313*(3), 145-198.

Grocott, J., & Taylor, G. K. (2002). Magmatic arc fault systems, deformation partitioning and emplacement of granitic complexes in the Coastal Cordillera, north Chilean Andes (25 30'S to 27 00'S). *Journal of the Geological Society*, *159*(4), 425-443.

Grocott, J., Brown, M., Dallmeyer, R. D., Taylor, G. K., & Treloar, P. J. (1994). Mechanisms of continental growth in extensional arcs: An example from the Andean plate-boundary zone. *Geology*, *22*(5), 391-394.

Hacker, B. R., Ratschbacher, L., Webb, L., McWilliams, M. O., Ireland, T., Calvert, A., Dong, S., Wenk, H., & Chateigner, D. (2000). Exhumation of ultrahigh- pressure continental crust in east central China: Late Triassic- Early Jurassic tectonic unroofing. *Journal of Geophysical Research: Solid Earth*, 105(B6), 13339-13364.

Hamilton, W., & Myers, W. B. (1966). Cenozoic tectonics of the western United States. *Reviews of Geophysics*, *4*(4), 509-549.

Hamilton, W. B. (1988). Detachment faulting in the Death Valley region, California and Nevada. *Geologic and hydrologic investigations of a potential nuclear waste disposal site at Yucca Mountain, southern Nevada: US Geological Survey Bulletin*, *1790*, 51-85.

Harrison, T. M. (1982). Diffusion of ^{40}Ar in hornblende. *Contributions to Mineralogy and Petrology*, 78(3), 324-331.

Harrison, T. M., Yin, A., Grove, M., Lovera, O. M., Ryerson, F. J., & Zhou, X. (2000). The Zedong Window: A record of superposed Tertiary convergence in southeastern Tibet. *Journal of Geophysical Research: Solid Earth*, *105*(B8), 19211-19230.

Hinz, N., & Faulds, J. E. (2009). *The Eldorado dike swarm, Eldorado Mountains, southern Nevada – Accommodating upper crustal extension in the Colorado River extensional corridor*. Abstract presented at the American Geophysical Union Conference.

Hinz, N. H., Faulds, J. E., & Ramelli, A. R. (2012a*). Preliminary geologic map of the Ireteba Peaks quadrangle, Clark County, Nevada.* Nevada Bureau of Mines and Geology (Open-File Report 2012-09, scale 1:24,000).

Hinz, N. H., Faulds, J. E., & Ramelli, A. R. (2012b). *Preliminary geologic map of the north half of the Fourth of July Mountain quadrangle, Clark County, Nevada*. Nevada Bureau of Mines and Geology (Open-File Report 2012-08, scale 1:24,000).

Hirth, G., & Tullis, J. (1992). Dislocation creep regimes in quartz aggregates. *Journal of Structural Geology*, *14*(2), 145-159.

Hirth, G., Teyssier, C., & Dunlap, J. W. (2001). An evaluation of quartzite flow laws based on comparisons between experimentally and naturally deformed rocks. *International Journal of Earth Sciences*, *90*(1), 77-87.

Honn, D., & Smith, E. I. (2008). The mid-Miocene Wilson Ridge Pluton and River Mountains volcanic section, Lake Mead area of Nevada and Arizona; linking a volcanic and plutonic section. *GSA Field Guide*, 11, 1-20.

Howard, K. A., & John, B. E. (1987). Crustal extension along a rooted system of imbricate low-angle faults: Colorado River extensional corridor, California and Arizona. *Geological Society, London, Special Publications*, *28*(1), 299-311.

Hurley, P. M., & Fairbairn, H. W. (1952). Alpha-Radiation Damage in Zircon. *Journal of Applied Physics*, *23*(12), 1408-1408.

Ildefonse, B., Blackman, D. K., John, B. E., Ohara, Y., Miller, D. J., & MacLeod, C. J. (2007). Oceanic core complexes and crustal accretion at slow-spreading ridges. *Geology*, *35*(7), 623-626.

Jackson, J., McKenzie, D., Priestley, K., & Emmerson, B. (2008). New views on the structure and rheology of the lithosphere. *Journal of the Geological Society*, *165*(2), 453-465.

Jessell, M. W. (1987). Grain-boundary migration microstructures in a naturally deformed quartzite. *Journal of Structural Geology, 9*(8), 1007-1014.

Johnson, B. M. (2014). *Thermal and compositional evolution of the Mid-Miocene Searchlight magmatic system (Nevada, USA) as recorded in zircon* (Master's thesis). San José State University.

Kapp, J. D. A., Miller, C. F., & Miller, J. S. (2002). Ireteba pluton, Eldorado Mountains, Nevada: Late, deep-source, peraluminous magmatism in the Cordilleran Interior. *The Journal of geology*, *110*(6), 649-669.

Ketcham, R. A. (1996). Thermal models of core- complex evolution in Arizona and New Guinea: Implications for ancient cooling paths and present- day heat flow. *Tectonics*, *15*(5), 933-951.

Klepeis, K., Betka, P., Clarke, G., Fanning, M., Hervé, F., Rojas, L., Mpodozis, C., & Thomson, S. (2010). Continental underthrusting and obduction during the Cretaceous closure of the Rocas Verdes rift basin, Cordillera Darwin, Patagonian Andes. *Tectonics*, *29*(3).

Klepeis, K. A., Schwartz, J., Stowell, H., & Tulloch, A. (2016). Gneiss domes, vertical and horizontal mass transfer, and the initiation of extension in the hot lower-crustal root of a continental arc, Fiordland, New Zealand. *Lithosphere*, *8*(2), 116-140.

Kruhl, J. H., & Vernon, R. H. (2005). Syndeformational emplacement of a tonalitic sheet-complex in a Late-Variscan thrust regime: fabrics and mechanism of intrusion, Monte'e Senes, Northeastern Sardinia, Italy. *The Canadian Mineralogist, 43*(1), 387-407.

Lagabrielle, Y., Brovarone, A. V., & Ildefonse, B. (2015). Fossil oceanic core complexes recognized in the blueschist metaophiolites of Western Alps and Corsica. *Earth-Science Reviews*, *141*, 1-26.

Law, R. D. (1990). Crystallographic fabrics: a selective review of their applications to research in structural geology. *Geological Society, London, Special Publications*, 54(1), 335-352.

Law, R. D. (2014). Deformation thermometry based on quartz c-axis fabrics and recrystallization microstructures: A review. *Journal of Structural Geology, 66*, 129-161.

Lenardic, A., Moresi, L., & Mühlhaus, H. (2000). The role of mobile belts for the longevity of deep cratonic lithosphere: the crumple zone model. *Geophysical Research Letters*, *27*(8), 1235-1238.

Lister, G. S., & Davis, G. A. (1989). The origin of metamorphic core complexes and detachment faults formed during Tertiary continental extension in the northern Colorado River region, USA. *Journal of Structural Geology*, *11*(1-2), 65-94.

Lister, G. S., & Dornsiepen, U. F. (1982). Fabric transitions in the Saxony granulite terrain. *Journal of Structural Geology*, 4(1), 81-92.

Lloyd, G. E., & Freeman, B. (1994). Dynamic recrystallization of quartz under greenschist conditions. *Journal of Structural Geology, 16*(6), 867-881.

Mainprice, D., Bouchez, J. L., Blumenfeld, P., & Tubià, J. M. (1986). Dominant c slip in naturally deformed quartz: Implications for dramatic plastic softening at high temperature. *Geology*, 14(10), 819-822.

Malavieille, J. (1987). Extensional shearing deformation and kilometer-scale “a”-type folds in a Cordilleran Metamorphic Core Complex (Raft River Mountains, northwestern Utah). *Tectonics*, *6*(4), 423-448.

Mattauer, M. (1975). Sur le mécanisme de formation de la schistosité dans l'Himalaya. *Earth and Planetary Science Letters, 28*(2), 144-154.

McKenzie, D. (1978). Some remarks on the development of sedimentary basins. *Earth and Planetary science letters*, *40*(1), 25-32.

Metcalf, R. V., Smith, E. I., Walker, J. D., Reed, R. C., & Gonzales, D. A. (1995). Isotopic disequilibrium among commingled hybrid magmas: evidence for a two-stage magma mixing-commingling process in the Mt. Perkins Pluton, Arizona. *The Journal of Geology*, *103*(5), 509-527.

Miller, C. F., & Miller, J. S. (2002). Contrasting stratified plutons exposed in tilt blocks, Eldorado Mountains, Colorado River Rift, NV, USA. *Lithos*, *61*(3), 209-224.

Miller, R. B., & Paterson, S. R. (2001). Construction of mid-crustal sheeted plutons: Examples from the North Cascades, Washington. *Geological Society of America Bulletin*, *113*(11), 1423-1442.

Miller, J., Miller, C., Wooden, J., Perrault, D., Hodge, K., Faulds, J., Cates, N. & Means, M. (2006). *A 2 million year history of plutonism and volcanism in the searchlight magma system, Eldorado Mountains, Nevada (USA)*. Abstract presented at the American Geophysical Union conference.

Miller, E. L., Gans, P. B., & Garing, J. (1983). The Snake Range decollement: An exhumed mid-Tertiary ductile-brittle transition. *Tectonics*, *2*(3), 239-263.

Miller, C. F., Furbish, D. J., Walker, B. A., Claiborne, L. L., Koteas, G. C., Bleick, H. A., & Miller, J. S. (2011). Growth of plutons by incremental emplacement of sheets in crystal-rich host: Evidence from Miocene intrusions of the Colorado River region, Nevada, USA. *Tectonophysics*, *500*(1-4), 65-77.

Molnar, P., & Lyon-Caen, H. (1988). Some simple physical aspects of the support, structure, and evolution of mountain belts. *Processes in continental lithospheric deformation*, *218*, 179-207.

Molnar, P., Boos, W. R., & Battisti, D. S. (2010). Orographic controls on climate and paleoclimate of Asia: thermal and mechanical roles for the Tibetan Plateau. *Annual Review of Earth and Planetary Sciences*, *38*.

Molnar, P. (1992). Brace-Goetze strength profiles, the partitioning of strike-slip and thrust faulting at zones of oblique convergence, and the stress-heat flow paradox of the San Andreas fault. *International Geophysics*, *51*, 435-459.

Nabelek, P. I., Hofmeister, A. M., & Whittington, A. G. (2012). The influence of temperature-dependent thermal diffusivity on the conductive cooling rates of plutons and temperature-time paths in contact aureoles. *Earth and Planetary Science Letters*, *317*, 157-164.

Nasdala, L., Reiners, P. W., Garver, J. I., Kennedy, A. K., Stern, R. A., Balan, E., & Wirth, R. (2004). Incomplete retention of radiation damage in zircon from Sri Lanka. *American Mineralogist*, *89*(1), 219-231.

Nevitt, J. M., Warren, J. M., Kidder, S., & Pollard, D. D. (2017). Comparison of thermal modeling, microstructural analysis, and Ti-in-quartz thermobarometry to constrain the

thermal history of a cooling pluton during deformation in the Mount Abbot Quadrangle, CA. *Geochemistry, Geophysics, Geosystems*, *18*(3), 1270-1297.

Norton, D. (1979). Transport phenomena in hydrothermal systems: the redistribution of chemical components around cooling magmas. *Bull. Mineral*, *102*, 471-486.

Orme, D. A., Guenthner, W. R., Laskowski, A. K., & Reiners, P. W. (2016). Long-term tectonothermal history of Laramide basement from zircon–He age-eU correlations. *Earth and Planetary Science Letters*, *453*, 119-130.

Olive, J. A., Behn, M. D., & Tucholke, B. E. (2010). The structure of oceanic core complexes controlled by the depth distribution of magma emplacement. *Nature Geoscience*, *3*(7), 491.

Passchier, C. W. (1982). Pseudotachylyte and the development of ultramylonite bands in the Saint-Barthelemy Massif, French Pyrenees. *Journal of Structural Geology, 4*(1), 69-79.

Passchier, C. W., & Simpson, C. (1986). Porphyroclast systems as kinematic indicators. *Journal of Structural Geology, 8*(8), 831-843.

Paterson, S. R., Pignotta, G. S., & Vernon, R. H. (2004). The significance of microgranitoid enclave shapes and orientations. *Journal of Structural Geology, 26*(8), 1465-1481.

Paterson, S. R., & Fowler, T. K. (1993). Re-examining pluton emplacement processes. *Journal of Structural Geology*, *15*(2), 191-206.

Paterson, S. R., Fowler, T. K., Schmidt, K. L., Yoshinobu, A. S., Yuan, E. S., & Miller, R. B. (1998). Interpreting magmatic fabric patterns in plutons. *Lithos*, *44*(1), 53-82.

Paterson, S. R., Vernon, R. H., & Tobisch, O. T. (1989). A review of criteria for the identification of magmatic and tectonic foliations in granitoids. *Journal of Structural Geology*, *11*(3), 349–363.

Petford, N., Cruden, A. R., McCaffrey, K. J. W., & Vigneresse, J. L. (2000). Granite magma formation, transport and emplacement in the Earth's crust. *Nature*, *408*(6813), 669-673.

Platt, J. P. (2015). Rheology of two-phase systems: A microphysical and observational approach. *Journal of Structural Geology*, *77*, 213-227.

Platt, J. P., Behr, W. M., & Cooper, F. J. (2015). Metamorphic core complexes: windows into the mechanics and rheology of the crust. *Journal of the Geological Society*, *172*(1), 9-27.

Post, A., & Tullis, J. (1999). A recrystallized grain size piezometer for experimentally deformed feldspar aggregates. *Tectonophysics*, *303*(1-4), 159-173.

Proffett Jr, J. M. (1977). Cenozoic geology of the Yerington district, Nevada, and implications for the nature and origin of Basin and Range faulting. *Geological Society of America Bulletin*, *88*(2), 247-266.

Pryer, L. L. (1993). Microstructures in feldspars from a major crustal thrust zone: the Grenville Front, Ontario, Canada. *Journal of structural Geology*, *15*(1), 21-36.

Reich, M., Ewing, R. C., Ehlers, T. A., & Becker, U. (2007). Low-temperature anisotropic diffusion of helium in zircon: implications for zircon (U–Th)/He thermochronometry. *Geochimica et Cosmochimica Acta*, *71*(12), 3119-3130.

Reiners, P. W. (2005). Zircon (U-Th)/He thermochronometry. *Reviews in Mineralogy and Geochemistry*, *58*(1), 151-179.

Reiners, P. W., Farley, K. A., & Hickes, H. J. (2002). He diffusion and (U–Th)/He thermochronometry of zircon: initial results from Fish Canyon Tuff and Gold Butte. *Tectonophysics*, *349*(1), 297-308.

Reiners, P. W., Spell, T. L., Nicolescu, S., & Zanetti, K. A. (2004). Zircon (U-Th)/He thermochronometry: He diffusion and comparisons with 40 Ar/39 Ar dating. *Geochimica et cosmochimica acta*, *68*(8), 1857-1887.

Renne, P. R., Swisher, C. C., Deino, A. L., Karner, D. B., Owens, T. L., & DePaolo, D. J. (1998). Intercalibration of standards, absolute ages and uncertainties in 40Ar/39Ar dating. *Chemical Geology*, *145*(1-2), 117-152.

Rey, P. F., Teyssier, C., & Whitney, D. L. (2009). Extension rates, crustal melting, and core complex dynamics. *Geology*, *37*(5), 391-394.

Rubin, A. E., Cooper, K. M., Till, C. B., Kent, A. J., Costa, F., Bose, M., Gravley, D., Deering, C., & Cole, J. (2017). Rapid cooling and cold storage in a silicic magma reservoir recorded in individual crystals. *Science*, *356*(6343), 1154-1156.

Rudnick, R. L., & Fountain, D. M. (1995). Nature and composition of the continental crust: a lower crustal perspective. *Reviews of geophysics*, *33*(3), 267-309.

Ruppert, R.F., & Faulds, J.E., 1998, *Geologic map of the western half of the Fourth of July Mountain Quadrangle, southern Nevada*. Nevada Bureau of Mines and Geology (Open-File Report 98–7, scale 1:24 000).

Ruppert, R.F., 1999, *Stratigraphic and structural framework of the northern Newberry Mountains, southern Nevada: Assessing the interplay between magmatism and extension* (Master's thesis). Iowa City, University of Iowa.

Schulmann, K., Lexa, O., Štípská, P., Racek, M., Tajčmanová, L., Konopásek, J., ... & Lehmann, J. (2008). Vertical extrusion and horizontal channel flow of orogenic lower crust: key exhumation mechanisms in large hot orogens?. *Journal of metamorphic Geology*, 26(2), 273-297.

Singleton, J. S., Stockli, D. F., Gans, P. B., & Prior, M. G. (2014). Timing, rate, and magnitude of slip on the Buckskin-Rawhide detachment fault, west central Arizona. *Tectonics*, *33*(8), 1596-1615.

Smith, E. I., & Faulds, J. E. (1994). *Patterns of Miocene magmatism in the northern Colorado River extensional corridor (NCREC).* Abstract presented at the Geological Society of America conference.

Snoke, A. W., Howard, K. A., McGrew, A. J., Burton, B. R., Barnes, C. G., Peters, M. T., and Wright, J. E. (1997) The Grand Tour of the Ruby-East Humboldt Metamorphic Core complex, Northeastern Nevada: Part 1-Introduction & Road Log. *Brigham Young University Geology Studies*, 42.

Spencer, J. E., Richard, S. M., Reynolds, S. J., Miller, R. J., Shafiqullah, M., Gilbert, W. G., & Grubensky, M. J. (1995). Spatial and temporal relationships between mid-Tertiary magmatism and extension in southwestern Arizona. *Journal of Geophysical Research: Solid Earth*, *100*(B6), 10321-10351.

Spencer, J. E. (1984). Role of tectonic denudation in warping and uplift of low-angle normal faults. *Geology, 12*(2), 95-98.

Staudacher, T., Jessberger, E. K., Dorflinger, D., & Kiko, J. (1978). A refined ultrahigh-vacuum furnace for rare gas analysis. *Journal of Physics E: Scientific Instruments, 11*(8), 781.

Stewart, J. H. (1978). Basin-range structure in western North America: A review. *Geological Society of America Memoirs*, *152*, 1-32.

Stewart, J. H. (1980). Regional tilt patterns of late Cenozoic basin-range fault blocks, western United States. *Geological Society of America Bulletin*, *91*(8), 460-464.

Stipp, M., & Tullis, J. (2003). The recrystallized grain size piezometer for quartz. *Geophysical Research Letters*, *30*(21).

Stipp, M., StuÈnitz, H., Heilbronner, R., & Schmid, S. M. (2002). The eastern Tonale fault zone: a 'natural laboratory'for crystal plastic deformation of quartz over a temperature range from 250 to 700 C. *Journal of Structural Geology*, *24*(12), 1861-1884.

Stockli, D. F., Farley, K. A., & Dumitru, T. A. (2000). Calibration of the apatite (U-Th)/He thermochronometer on an exhumed fault block, White Mountains, California. *Geology*, *28*(11), 983-986.

Stockli, D. F. (2005). Application of low-temperature thermochronometry to extensional tectonic settings. *Reviews in Mineralogy and Geochemistry*, *58*(1), 411-448.

Taylor Jr, H. P. (1990). Oxygen and hydrogen isotope constraints on the deep circulation of surface waters into zones of hydrothermal metamorphism and melting. *The role of fluids in crustal processes*, *72*, 95.

Thigpen, J. R., Law, R. D., Lloyd, G. E., & Brown, S. J. (2010). Deformation temperatures, vorticity of flow, and strain in the Moine thrust zone and Moine nappe: Reassessing the tectonic evolution of the Scandian foreland–hinterland transition zone. *Journal of Structural Geology, 32*(7), 920-940.

Tucholke, B. E., Behn, M. D., Buck, W. R., & Lin, J. (2008). Role of melt supply in oceanic detachment faulting and formation of megamullions. *Geology*, *36*(6), 455-458.

Tsurumi, J., Hosonuma, H., & Kanagawa, K. (2003). Strain localization due to a positive feedback of deformation and myrmekite-forming reaction in granite and aplite mylonites along the Hatagawa Shear Zone of NE Japan. *Journal of Structural Geology, 25*(4), 557-574.

Tullis, J., & Yund, R. A. (1985). Dynamic recrystallization of feldspar: A mechanism for ductile shear zone formation. *Geology*, *13*(4), 238-241.

Tullis, J., & Yund, R. A. (1991). Diffusion creep in feldspar aggregates: experimental evidence. *Journal of Structural Geology*, *13*(9), 987-1000.

Walker Jr, B. A., Miller, C. F., Claiborne, L. L., Wooden, J. L., & Miller, J. S. (2007). Geology and geochronology of the Spirit Mountain batholith, southern Nevada: Implications for timescales and physical processes of batholith construction. *Journal of Volcanology and Geothermal Research*, *167*(1-4), 239-262.

Wen, D. R., Liu, D., Chung, S. L., Chu, M. F., Ji, J., Zhang, Q., Song, B., Lee, T, Yeh, M., & Lo, C. H. (2008). Zircon SHRIMP U–Pb ages of the Gangdese Batholith and implications for Neotethyan subduction in southern Tibet. *Chemical Geology*, *252*(3), 191-201.

Wernicke, B., & Axen, G. J. (1988). On the role of isostasy in the evolution of normal fault systems. *Geology*, *16*(9), 848-851.

Wernicke, B., & Snow, J. K. (1998). Cenozoic tectonism in the central Basin and Range: Motion of the Sierran-Great Valley block. *International Geology Review, 40*(5), 403-410.

Wernicke, B. (1981). Low-angle normal faults in the Basin and Range Province: nappe tectonics in an extending orogen. *Nature, 291*(5817).

Wernicke, B., & Burchfiel, B. C. (1982). Modes of extensional tectonics. *Journal of Structural Geology*, *4*(2), 105-115.

Wernicke, B. (1985). Uniform-sense normal simple shear of the continental lithosphere. *Canadian Journal of Earth Sciences*, *22*(1), 108-125.

Wernicke, B. (1992). Cenozoic extensional tectonics of the western U.S. Cordillera In B. C. Burchfiel, P. W. Lipman, M. L. Zoback (Eds.*), The Cordilleran orogen: conterminous U.S.* (Vol. G-3, pp. 553-581). Boulder, CO: Geological Society of America.

Whittington, A. G., Hofmeister, A. M., & Nabelek, P. I. (2009). Temperature-dependent thermal diffusivity of the Earth's crust and implications for magmatism. *Nature*, *458*(7236), 319.

Wolfe, M. R., & Stockli, D. F. (2010). Zircon (U–Th)/He thermochronometry in the KTB drill hole, Germany, and its implications for bulk He diffusion kinetics in zircon. *Earth and Planetary Science Letters*, *295*(1-2), 69-82.

Žák, J., Verner, K., Holub, F. V., Kabele, P., Chlupáčová, M., & Halodová, P. (2012). Magmatic to solid state fabrics in syntectonic granitoids recording early Carboniferous orogenic collapse in the Bohemian Massif. *Journal of Structural Geology*, *36*, 27-42.

Zuza, A. V., Yin, A., Lin, J., & Sun, M. (2017). Spacing and strength of active continental strike-slip faults. *Earth and Planetary Science Letters*, *457*, 49-62.

Zuza, A. V., & Carlson, C. W. (2018). What can strike‐slip fault spacing tell us about the plate boundary of western North America?. *Terra Nova*, *30*(2), 105-113.

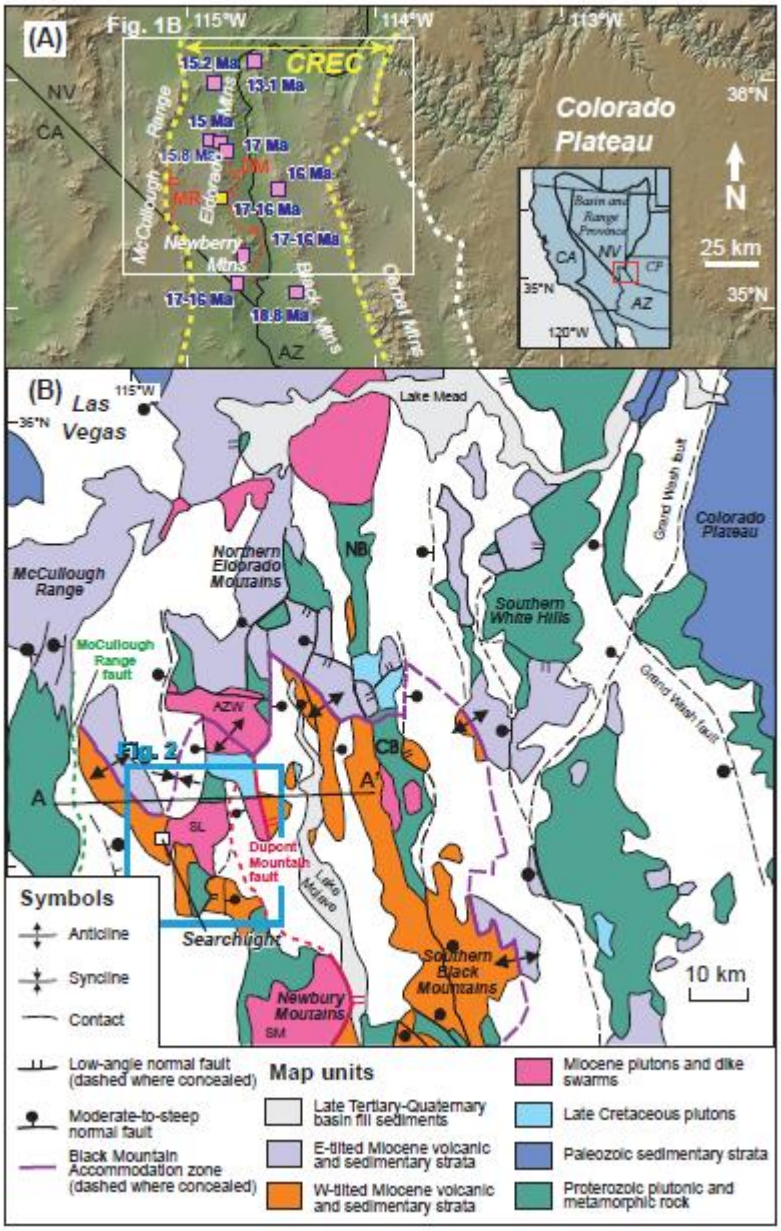

Figure 1. (A) Map showing the extent of the Colorado River extensional corridor (CREC), Miocene silicic magmatic centers (pink and blue squares, Searchlight is yellow) with age ranges, names of important ranges referred to in the text, and the two major north-striking normal faults discussed in this study, the McCullough Range (MR) and Dupont Mountain (DM) faults. Note that magmatism migrates northward, and extension generally followed shortly after magmatism. White box shows extent of Figure 1B. Inset shows the location of this map, encompassed in a red box, relative to the western U.S. (B) Generalized geologic map of the northern Colorado River extensional corridor. The east-directed Dupont-Mountain and McCullough Range faults are shown in red and green, respectively. Approximate cross-section line of model in Figure 13 is shown as A-A'. Blue box shows study area, and location of Figure 2. Acronyms: AZW—Aztec Wash pluton; SL—Searchlight pluton; SM—Spirit Mountain batholith; NB—Northern Black Mountains; CB—Central Black Mountains. Figures adapted from Faulds et al. (2001, 2002a) and Hinz and Faulds (2009).

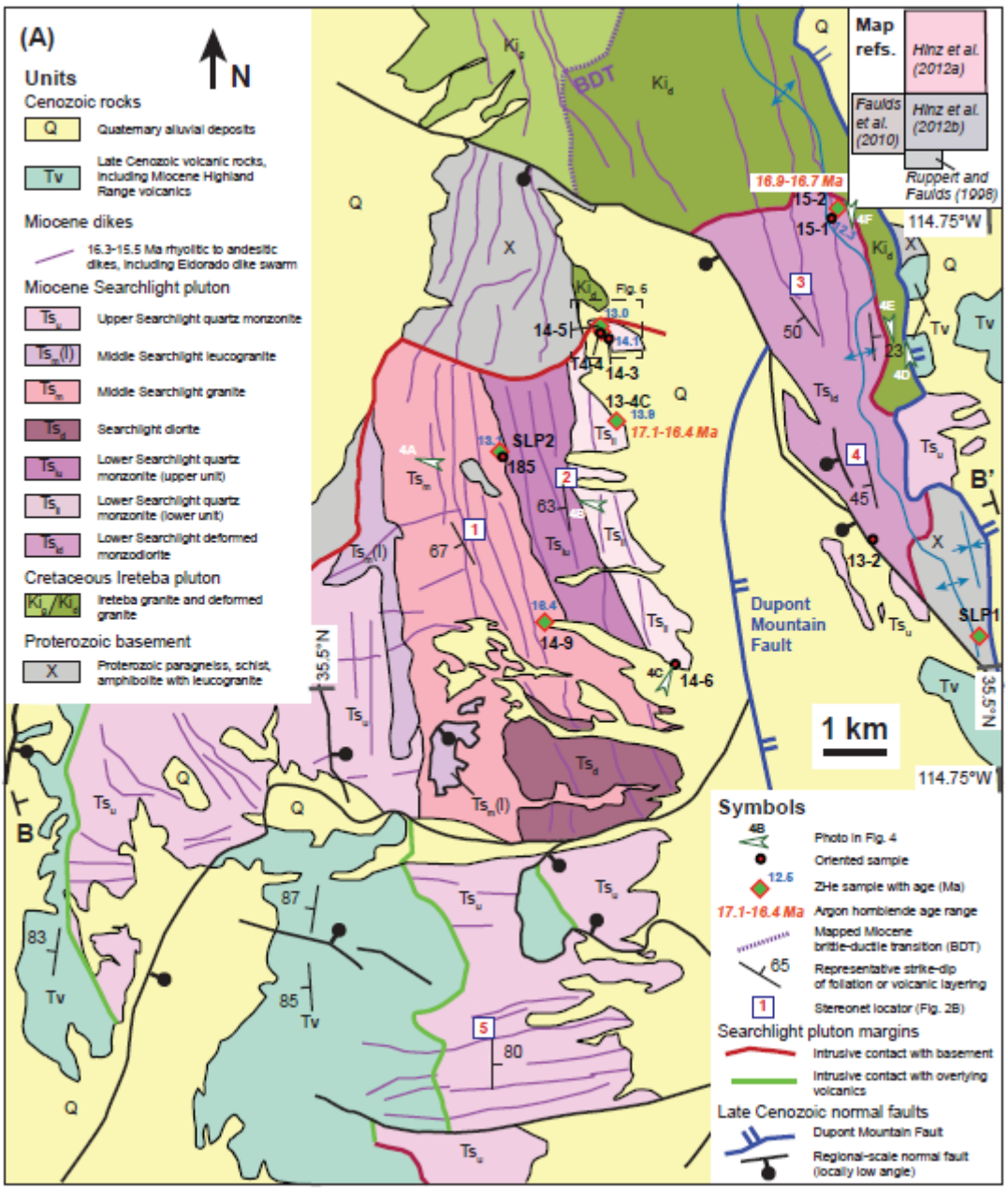

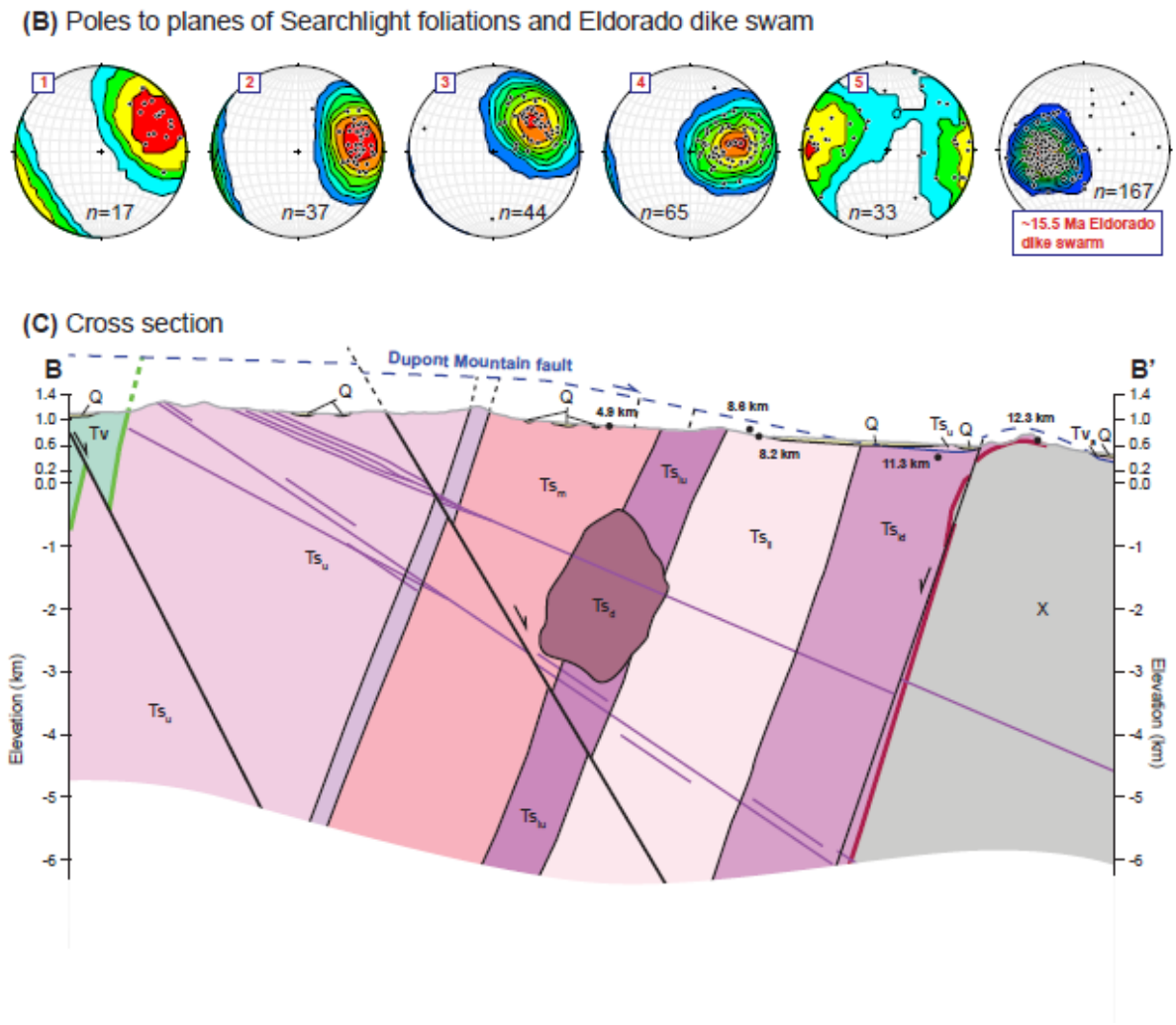

Figure 2. (A) Simplified geologic map, (B) stereographic projections of plutonic foliation and volcanic dikes, and (C) cross-section of the Searchlight pluton in southern Nevada. Inset in (A) shows 1:24,000 scale mapping sources. The map and cross section also show the location of samples from this study and the approximate locations of aluminum-in-hornblende pressure estimates (bold black numbers) from Bachl et al. (2001).

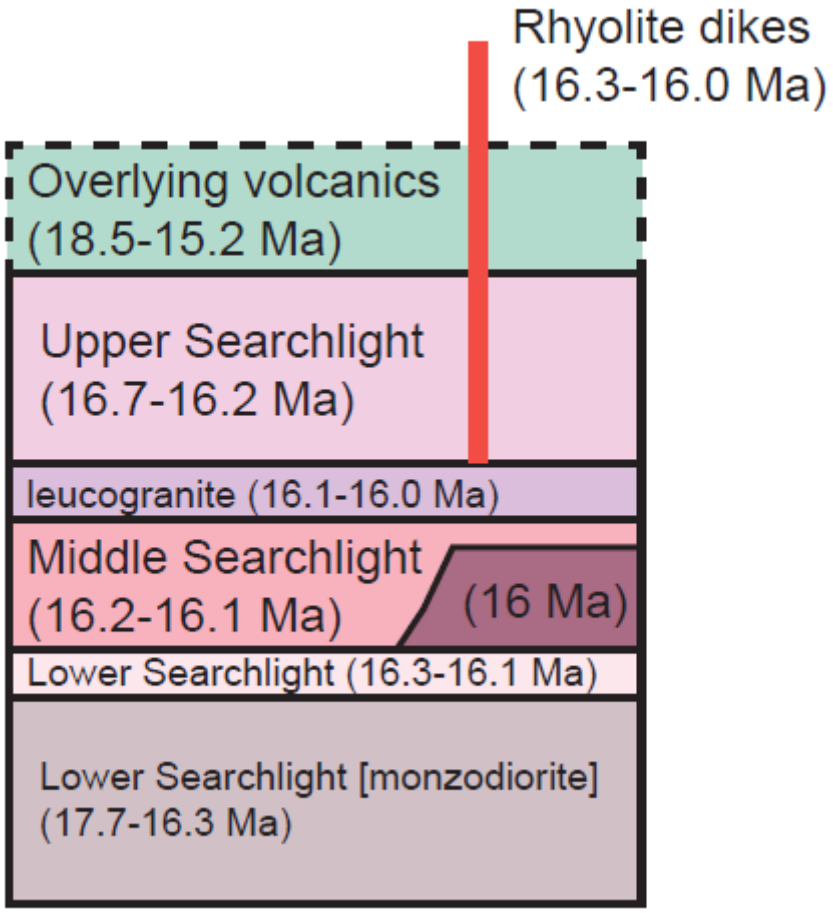

Figure 3. Simplified chronology of the Searchlight pluton units sourced from Bachl et al. (2001) and Johnson (2014).

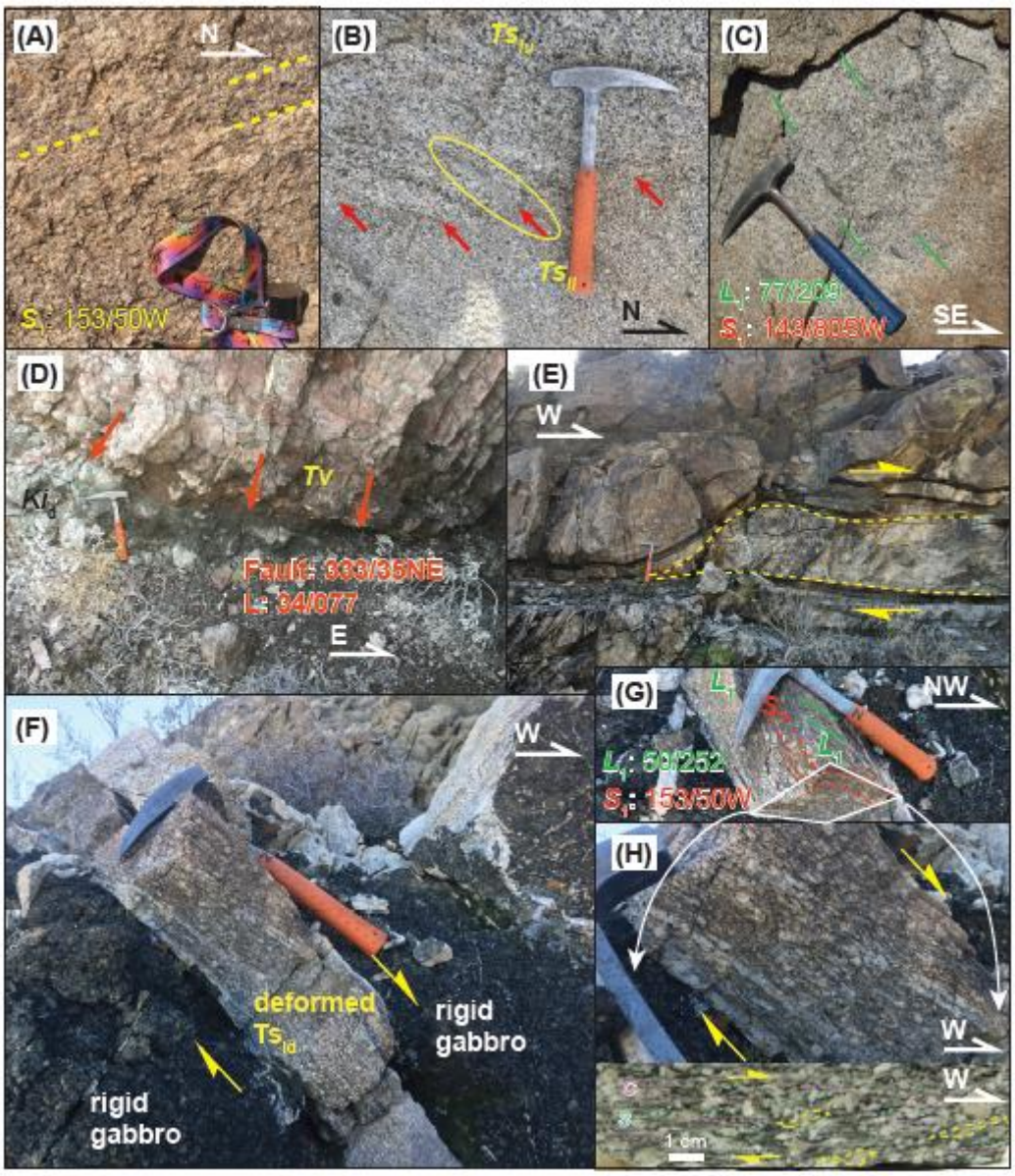

Figure 4. Field photographs; locations shown in Figure 2A. (A) Weakly developed fabrics in the uppermost Middle Searchlight pluton; note foliations (yellow dashed line) dip away in photo [location: 35.532N, 114.858W]. (B) Contact (red arrows) between the upper (Ts_{lu}) and lower (Ts_{ll}) units of the Lower Searchlight quartz monzonite unit, showing truncation of an elongate mafic enclave (yellow oval). [location: 35.524N, 114.827W]. (C) Looking at foliation surface at well-defined aligned-hornblende lineations. The alignment of euhedral-subhedral hornblende is interpreted as a magmatic lineation, whereas recrystallized tails and deformation textures of the feldspar grains are interpreted as overprinting sub-solidus fabrics.

Sample 14-6 was collected from this locality [location: 35.501N, 114.810W]. (D-H) Photographs from the eastern exposures from the Searchlight pluton (i.e., near its paleo-base). (D) Exposure of the Dupont Mountain fault placing Cenozoic volcanic rocks (Tv) over deformed Ireteba pluton (Ki_d) [location: 35.549N, 114.766W]. Here, a cataclastic breccia overprints mylonitic gneiss in the footwall, but both display top-east shear. Note that the top-east shear sense observed at this outcrop disappears moving toward the outcrop in Fig. 4E, located ~150 m to the west, where the dominant bottom-east, top-west shear sense is observed in the ductile fabrics, parallel to much of the Searchlight pluton to the west (E) Asymmetric boudinage in sub-Ts_{ld} unit, outlined with yellow dashed lines, with subhorizontal foliation, displaying top-west shear; C-S fabric in the outcrop displays similar kinematics [location: 35.549N, 114.768W]. (F-H) Outcrop of relatively rigid gabbro intruded by Ts_{ld} unit, which is strongly sheared eastside-up [location: 35.567N, 114.787W]. Inset in H shows sample slab cut from outcrop demonstrating bottom-east, eastside-up, shear sense based on asymmetric recrystallized mantle tails and S-C fabrics.

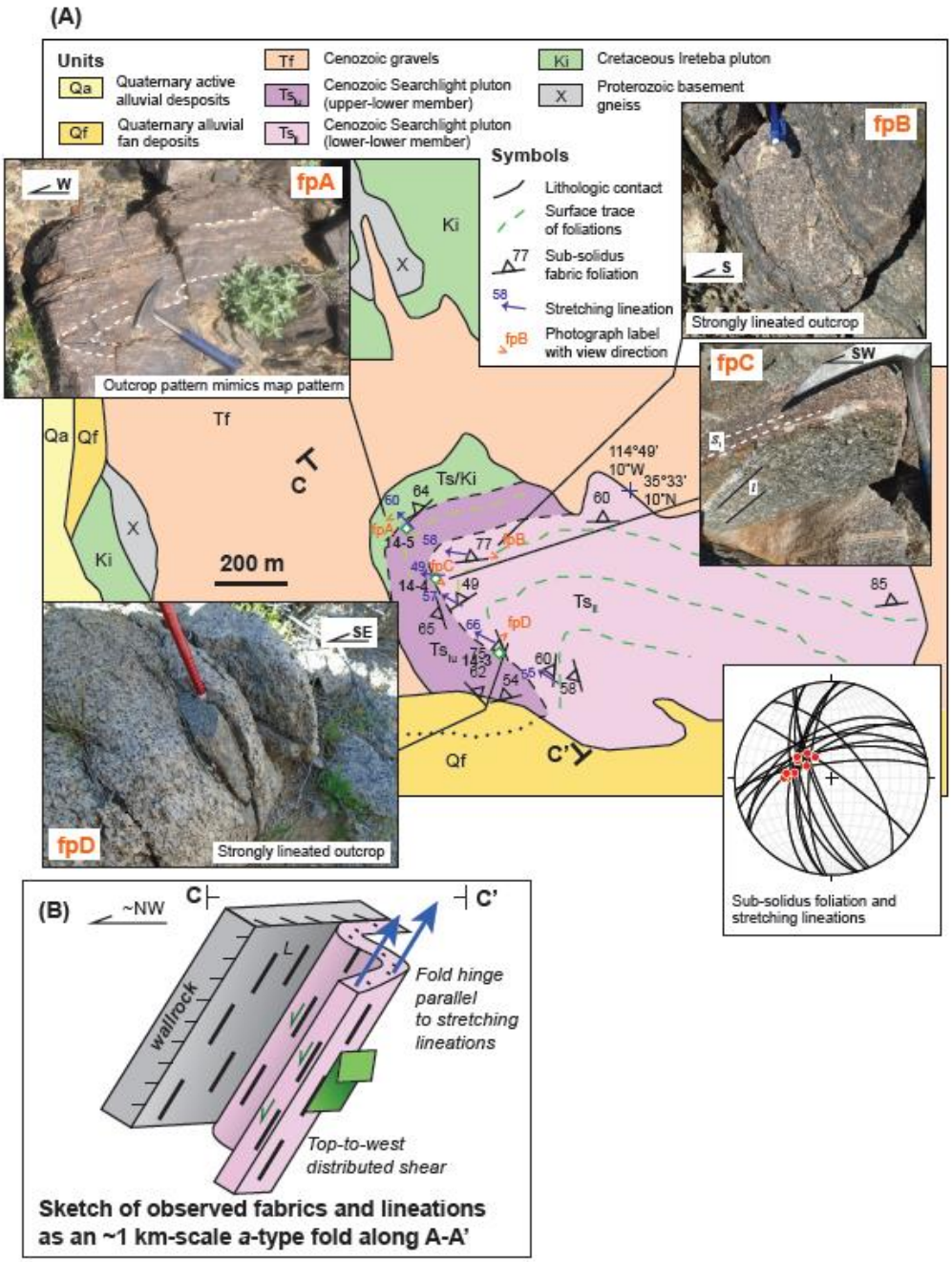

Figure 5. (A) Local geologic map along the northern margin of the Searchlight pluton and important field photographs (fp); inset stereonet plots sub-solidus foliations and stretching lineations. Note that the fabrics define a nearly vertical-axis asymmetric fold pair, which is parallel to outcrop-scale folds (e.g., fpA). Lineations in the outcrops parallel the fold hinges (see stereonet plot), which makes this fold an *a*-type fold (e.g., Mattauer, 1975; Malavieille, 1987; Hacker et al., 2000). (B) Sketch of relationship between outcrop pattern, fabrics, and lineations as an eastside-up *a*-type fold structure. These kinematics are also observed in thin-section scale (see **Figure 6**).

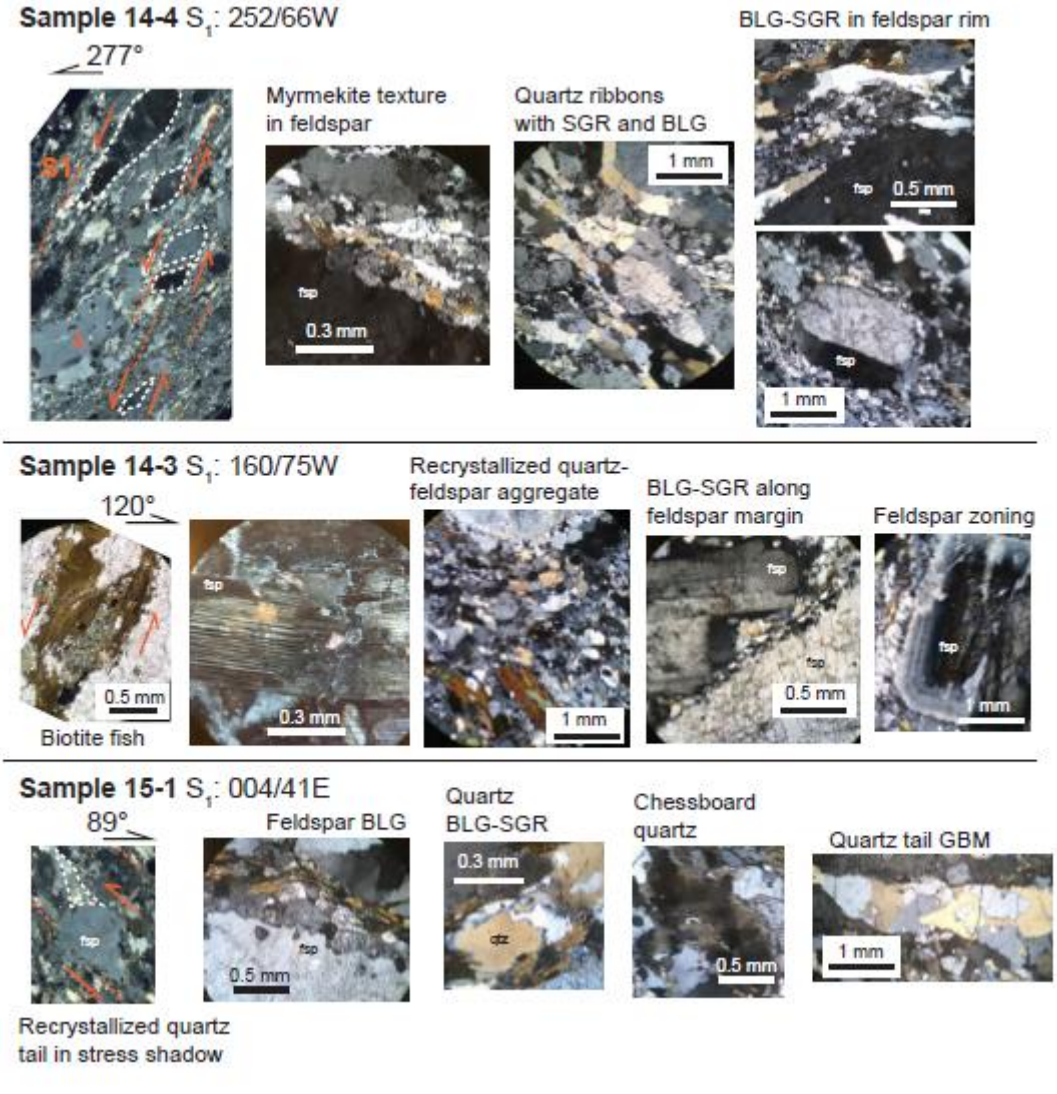

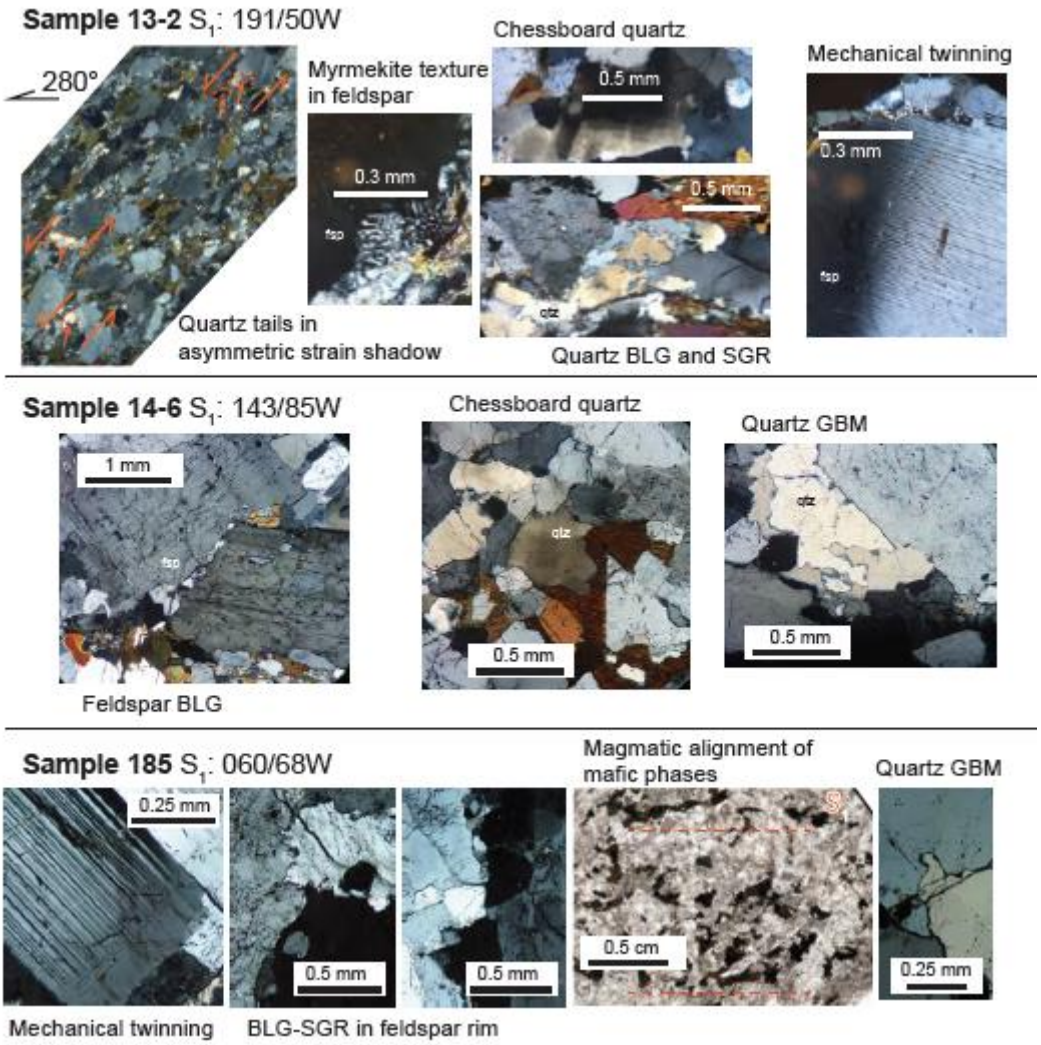

Figure 6. Photomicrographs of representative samples from across the Searchlight pluton showing deformation textures consistent with a progression from high temperature (i.e., magmatic) to low-temperature sub-solidus strain. Each sample shows signs of deformation over this large range of temperatures, but the samples are generally arranged in order from most intense sub-solidus strain to least, from top to bottom respectively. Samples and interpretations are discussed in more detail in the text. Red arrows for Sample 13-2 point out recrystallized quartz in strain shadows around feldspar grains; their asymmetry suggests eastside-up shear. BLG—Bulging recrystallization; SGR—Subgrain recrystallization; GMB—Grain-boundary migration recrystallization.

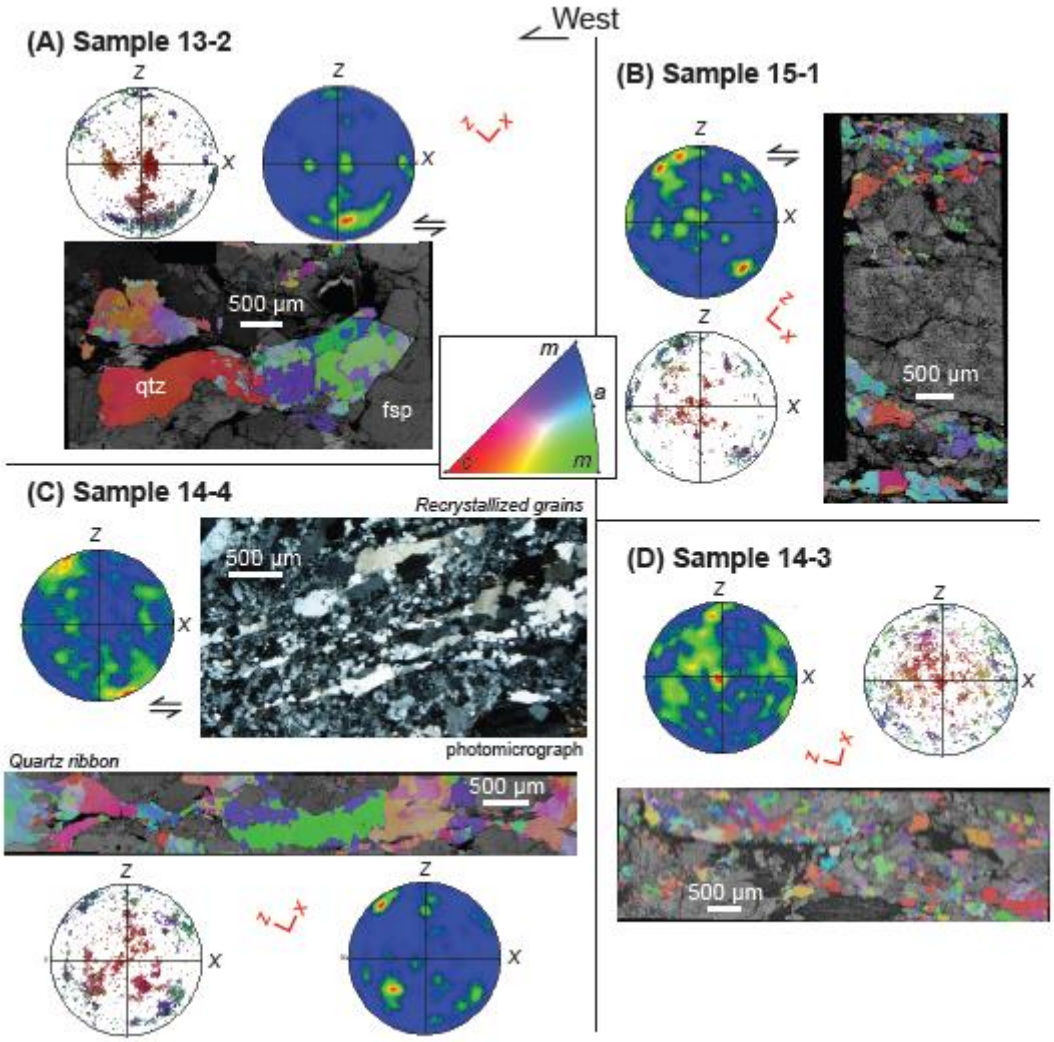

Figure 7. EBSD data from analyzed samples, including inverse-pole figure (IPF, legend in inset) maps for quartz grains with a band-contrast map for other phases and quartz *c*-axis pole figures (lower hemisphere, equal area projection). Note that the contoured pole figures are one analysis per grains, whereas the colored-coded point-pole figures are all analyses and correspond to the IPF maps. Sample 14-4 shows a cross-polar photomicrograph of recrystallized quartz grains. Plot-reference frames involve *Z* as the pole to the foliation plane and *X* as the lineation; red *Z*-*X* axes show approximate sample orientation relative to horizontal, as collected in the field (i.e., all west dipping except Sample 15-1).

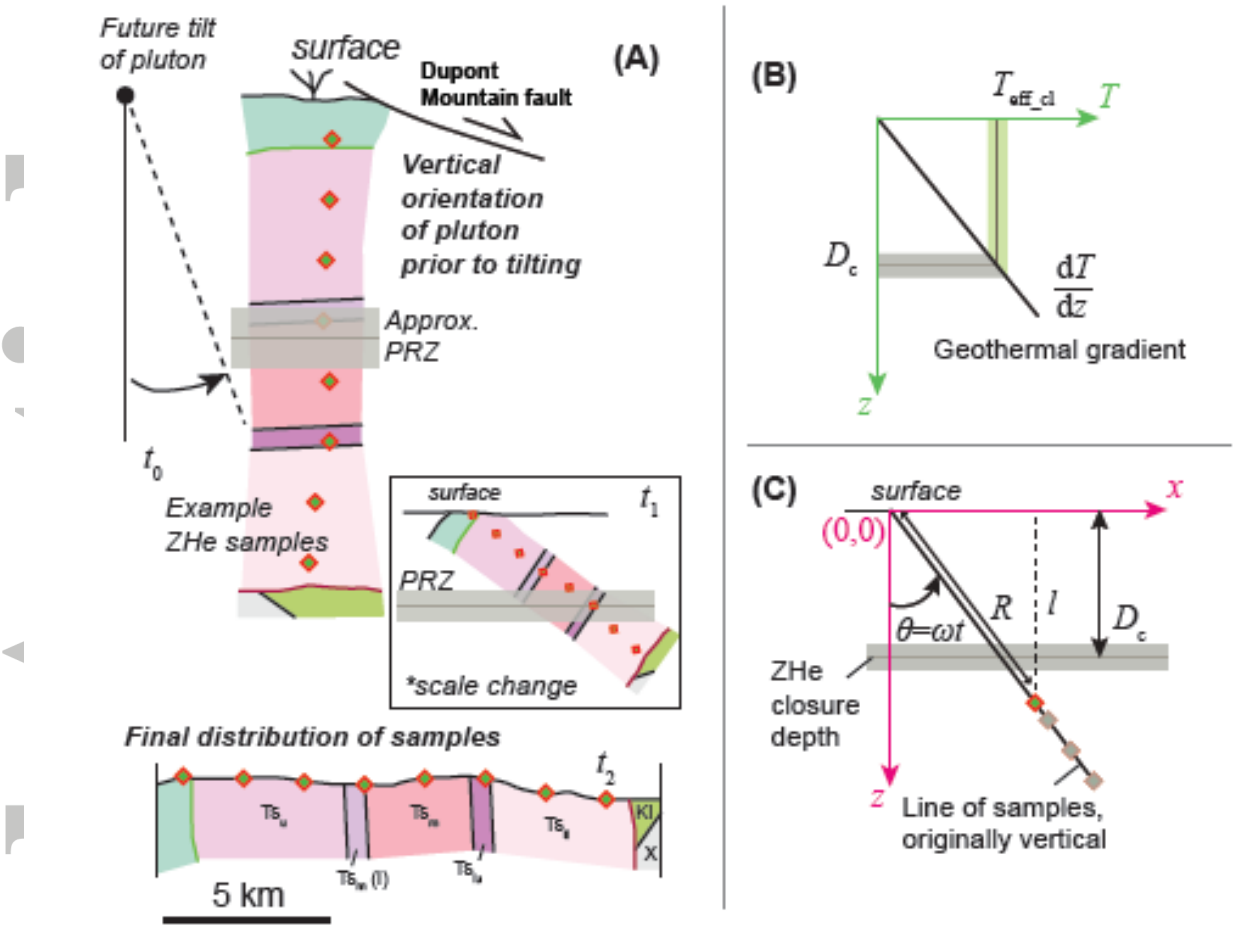

Figure 8. Setup for cooling model and thermochronology interpretation, as discussed in the text. (A) Restored, pre-rotation orientation of the pluton, at t_0, with the example sample locations and approximate partial retention zone (PRZ) for zircon helium dating. Extension causes the vertical section to rotate counter clockwise (in this perspective) during exhumation (see inset), at t_1. Schematic cross section of the Searchlight pluton today, at t_2, along the section line in Figure 2, showing example sampling traverse for ZHe analyses. (B) Relationship between the effective closure temperature T_{eff_cl} and the corresponding crustal depth of this temperature, D_c, based on an assumed geothermal gradient, dT/dz. (C) Definition of variables for the simple block-rotation cooling model discussed in the text.

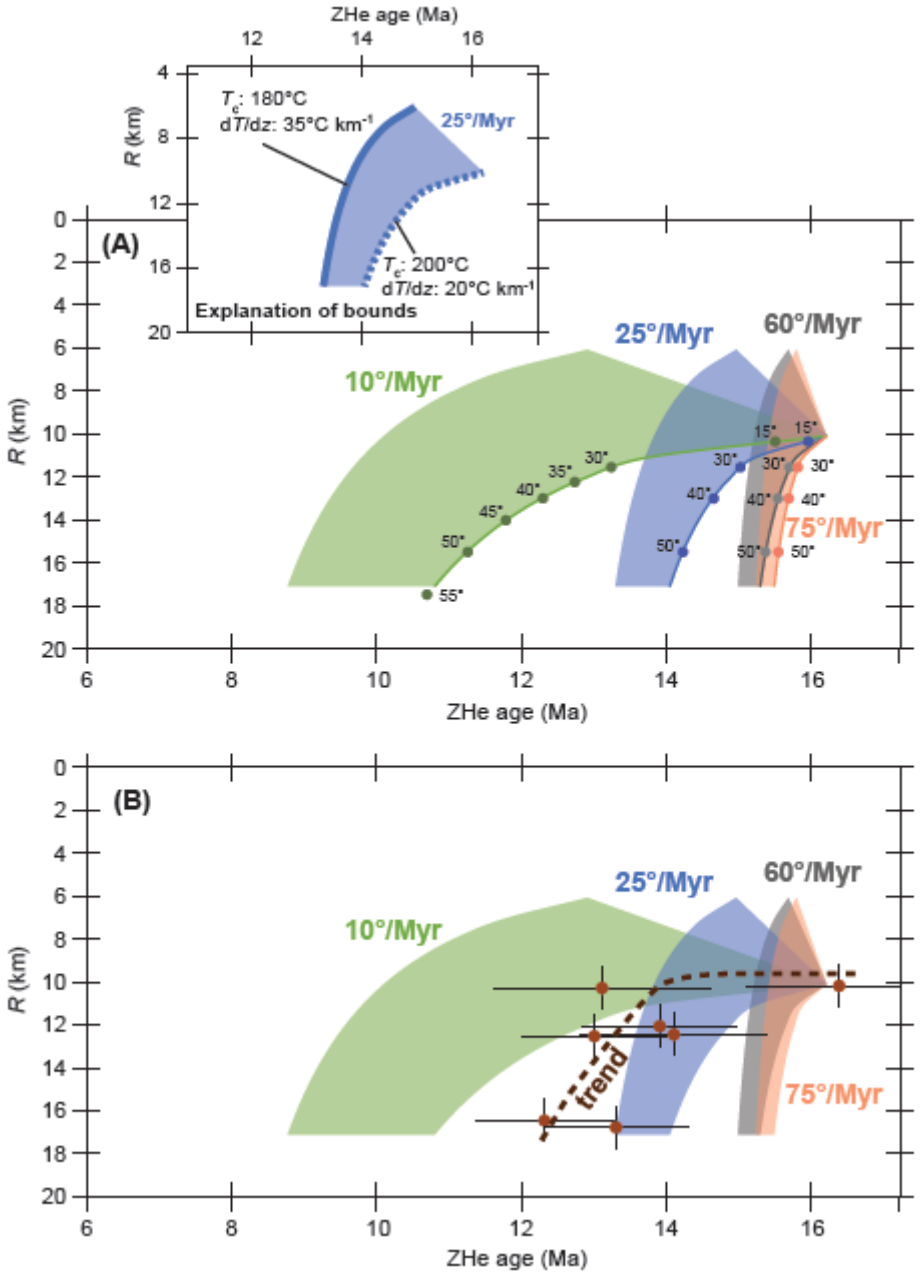

Figure 9. (A) Plot of predicted fields for *R* versus ZHe age given a range of geothermal gradients (20-35°C km^{-1}), closure temperatures (180-200°C), and rotation rates (i.e., 10° Myr^{-1}, 25° Myr^{-1}, 60° Myr^{-1}, and 75° Myr^{-1}). Inset shows how the upper field bound is set by the lower closure temperature and higher geothermal gradient whereas the lower field bound is controlled by the higher closure temperature and lower geothermal gradient. Also plotted are points demonstrating the tilting magnitude for a sample at a given *R* position required to reach ZHe closure temperature depths, assuming lower field boundary conditions (i.e., T_c=200°C; dT/dz=20°C/km). (B) Same plot as A, except overlain with our ZHe thermochronology observations. Weighted mean ages and *R* values provided in Table 2; a 1 km uncertainty was added to the *R* position for each data point.

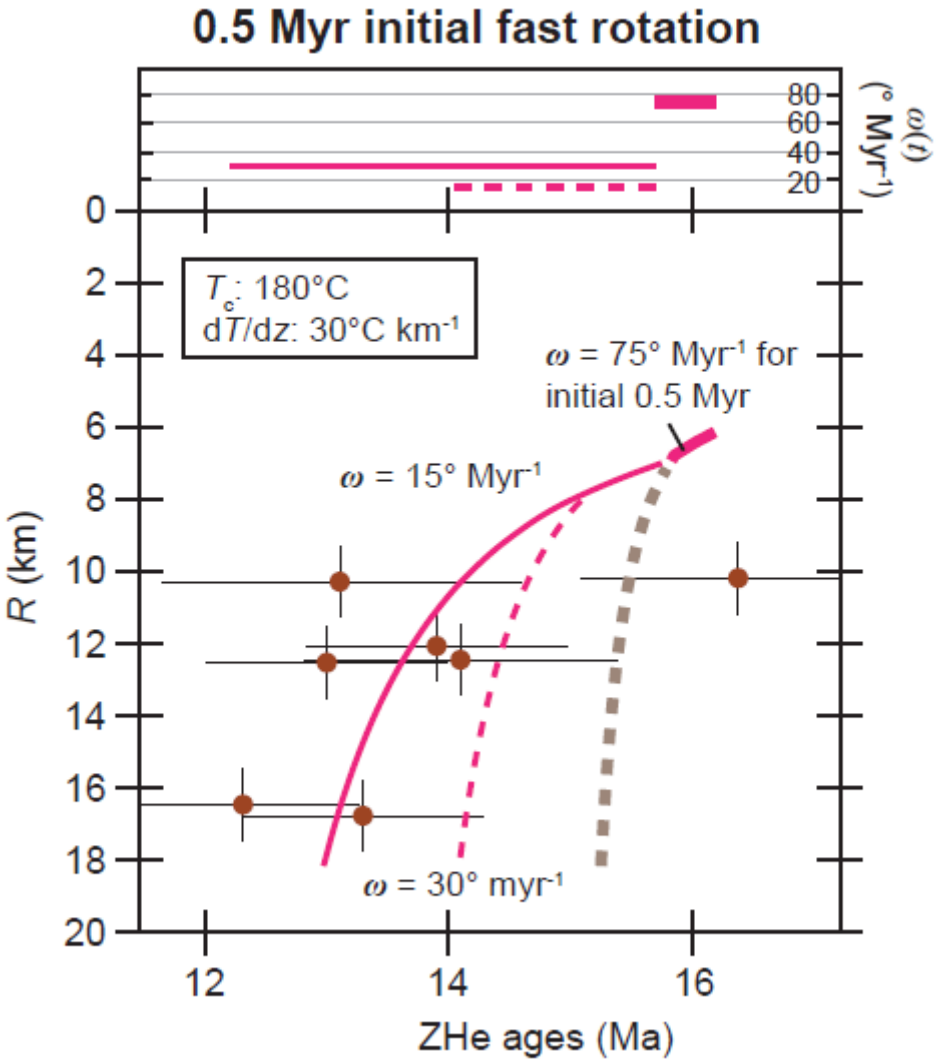

Figure 10. Plot of ZHe data with curves modeling predicted values for *R* and ZHe age, assuming rapid rotation (75° Myr^{-1}) for 0.5 Myr followed by slower rotation (i.e., 15° Myr^{-1} or 30° Myr^{-1}). These rotation rates are shown in the upper section of this plot. Model assumes one closure temperature (180°C) and geothermal gradient (30°C km^{-1}).

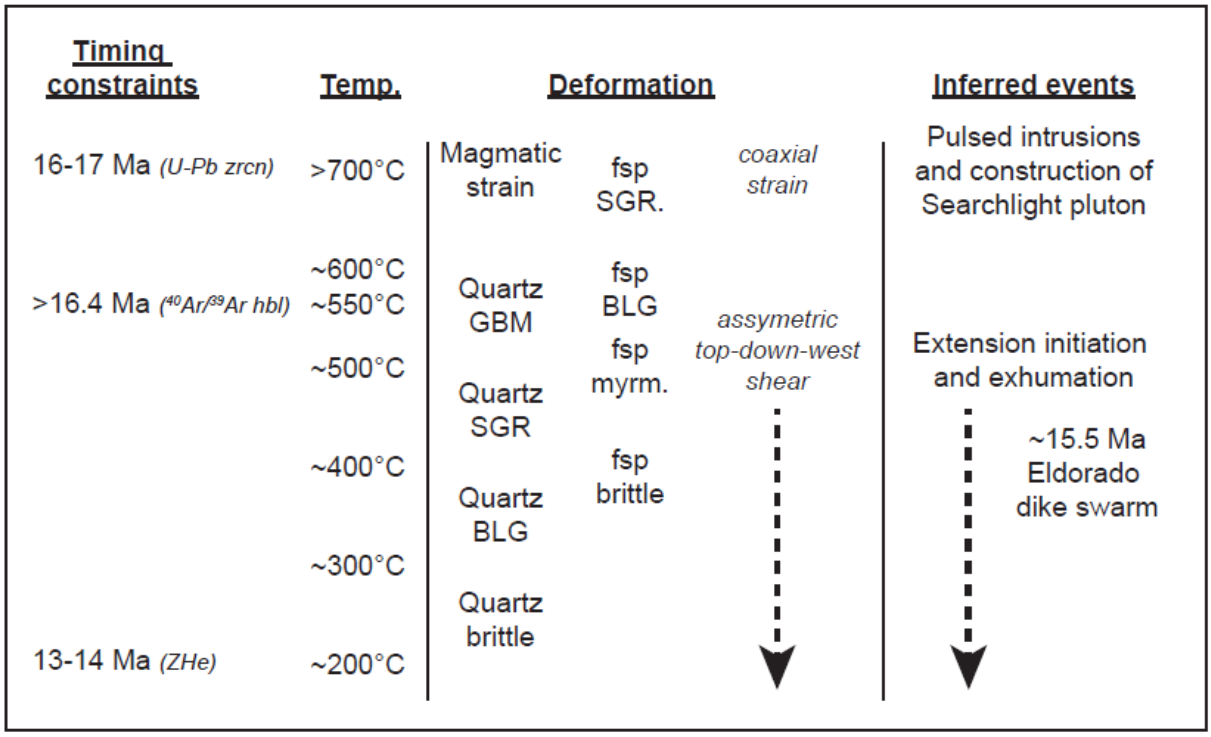

Figure 11. Summary of key timing constraints, deformation fabrics, inferred strain temperatures and interpreted tectonic events affecting the Searchlight pluton, as documented in this study. Zircon-age constraints from Johnson (2014). fsp—feldspar; myrm.—myrmekite texture

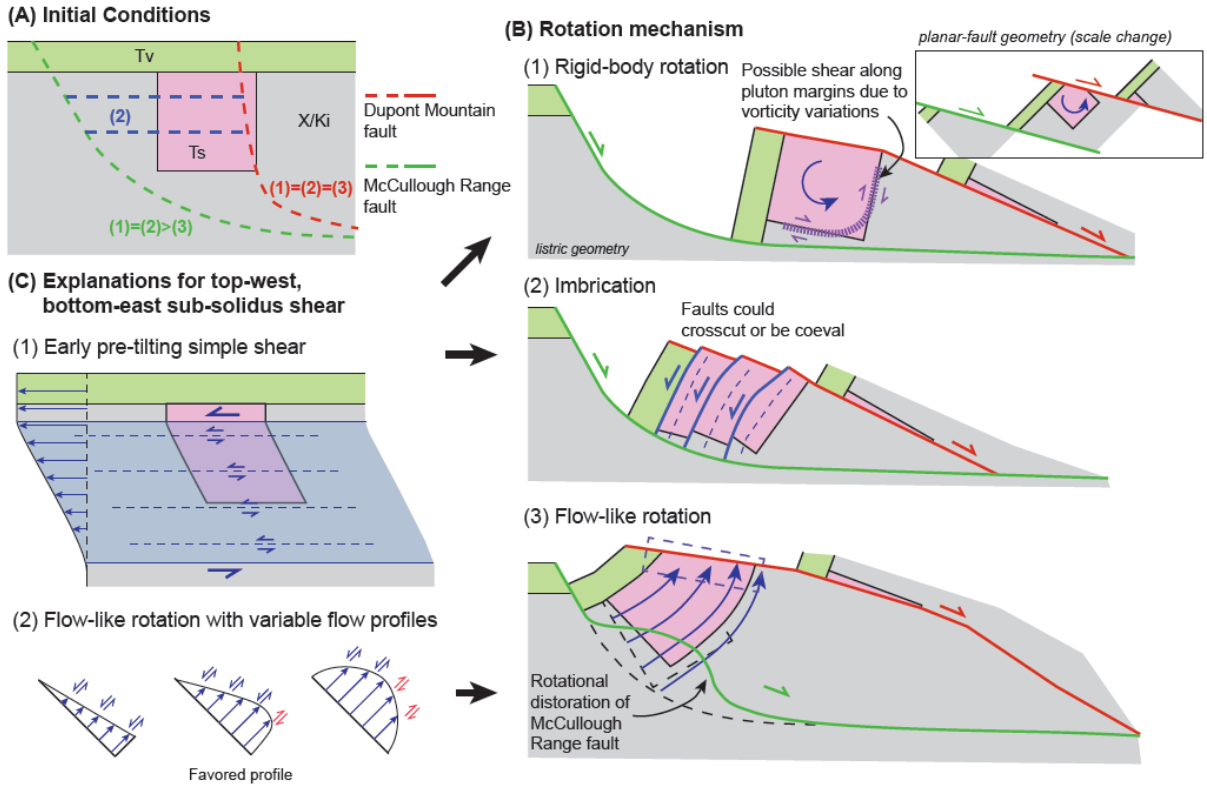

Figure 12. Postulated end-member models for tilting of the Searchlight pluton during extension, including (A) assumed initial conditions and (B) predicted fault geometries, offset magnitudes, and the shear sense of sub-solidus shear zones within the pluton. In A the numbers key the inferred faults to the specific models in panel B that require them, and their relative relationships (i.e., = or >) schematically suggest the importance of each structure for a given model. For example, imbrication model (2) requires more slip on the McCullough Range fault than flow-like rotation model (3), hence the green (2)>(3) next to this structure. Note that eastside-up shear restores to top-west shear prior to tilting, which could have originated from either (C) early top-west extensional strain or the flow-like rotational process.

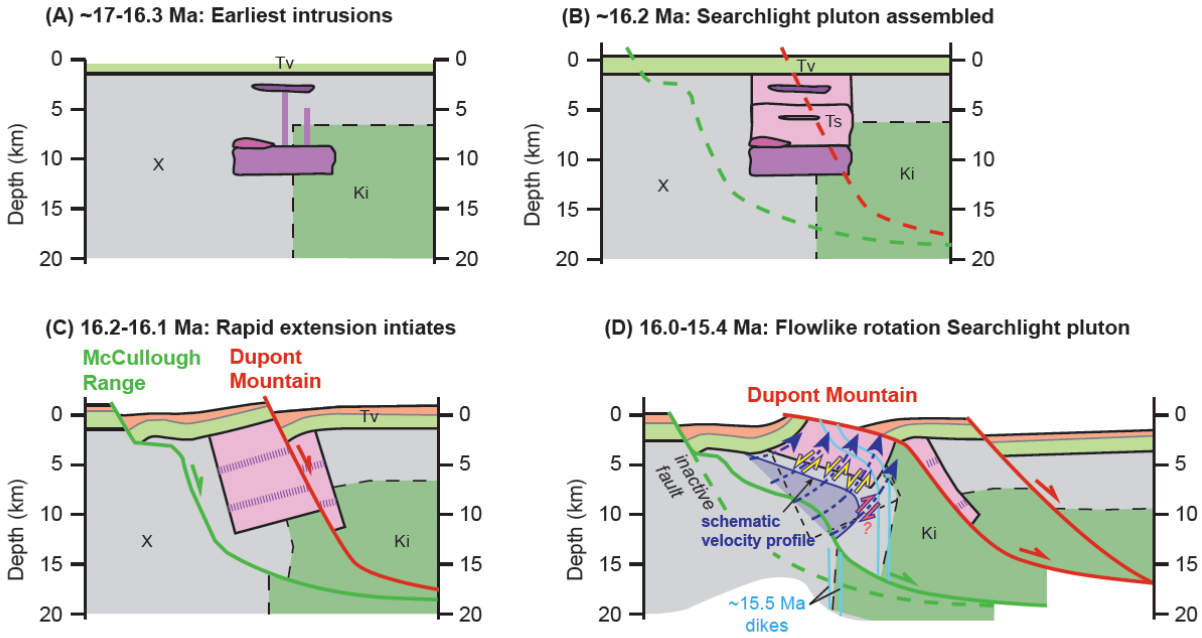

Figure 13. Tectonic model for the rotation of the Searchlight pluton in the context of regional east-west extension, and the relative involvement of the McCullough Range and Dupont Mountain faults. Model is drafted schematically along section line A-A' in Figure 2. A simplified intrusion history is assumed in this model. Rotational flow of the footwall is shown schematically, including the upwarping of the abandoned McCullough Range fault at depth. Note tilt fanning of the overlying volcanic rocks, but minor-offset steep normal faults are not shown. Vertical flow of the Dupont Mountain footwall is matched by erosion, such that relief in this region is insignificant.

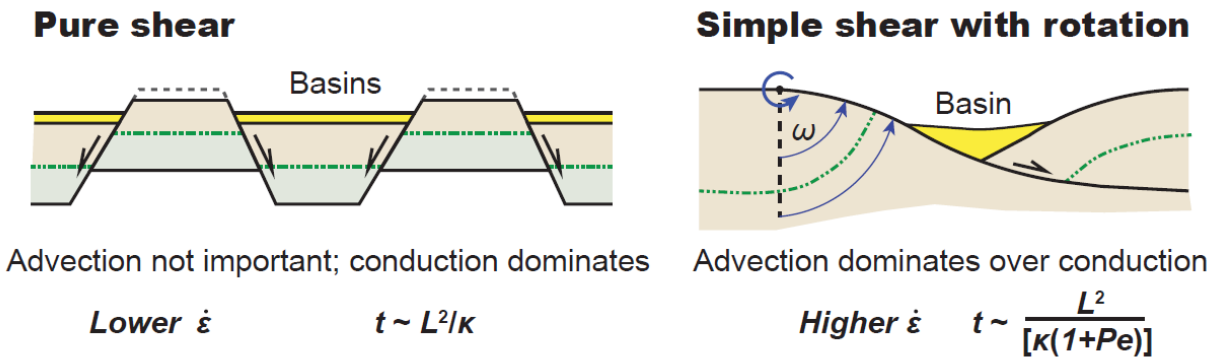

Figure 14. Sketch of two end-member modes of extension and their predicted characteristic cooling times. Dashed green line is a marker horizon. Variables: E—advection term that includes vertical motion and erosion; $\dot{\varepsilon}$—extensional strain rate; t—characteristic cooling time; L—characteristic length scale; κ—thermal diffusivity; Pe—Péclet number; ω—rotation rate.

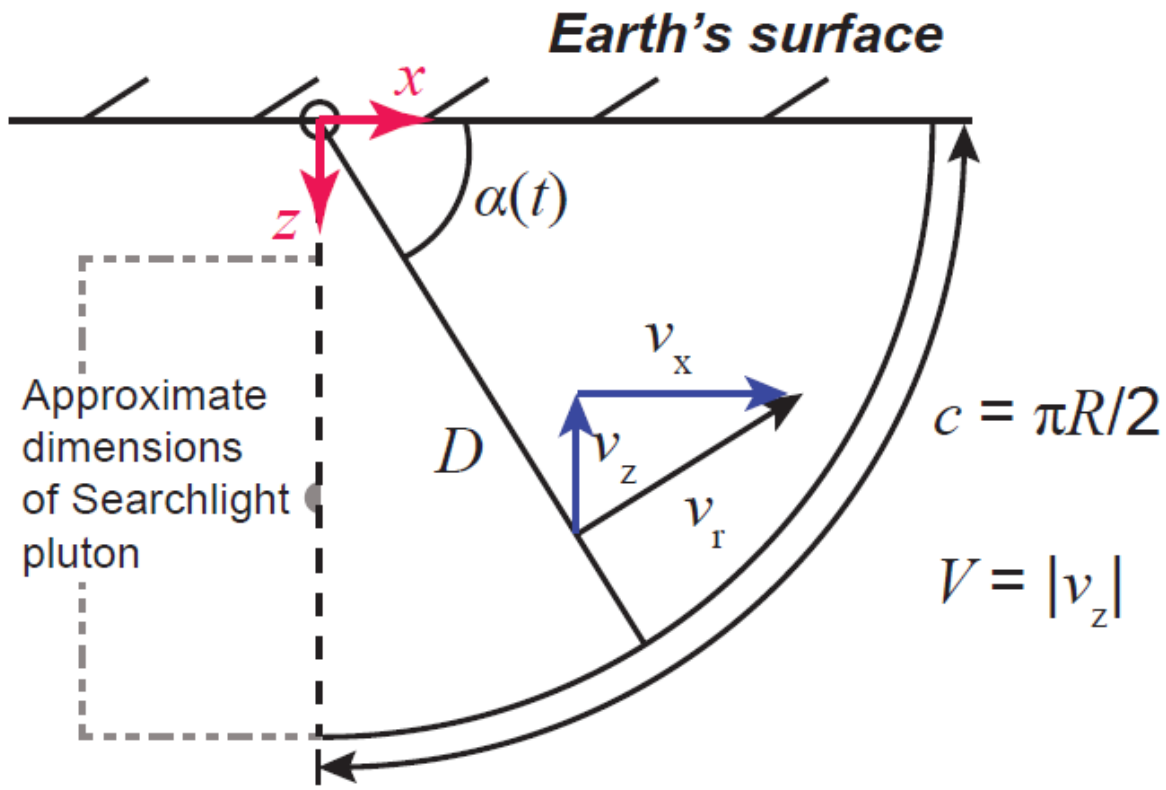

Figure 15. Setup for 2D kinematic model for vertical rock advection via horizontal axis rotation.

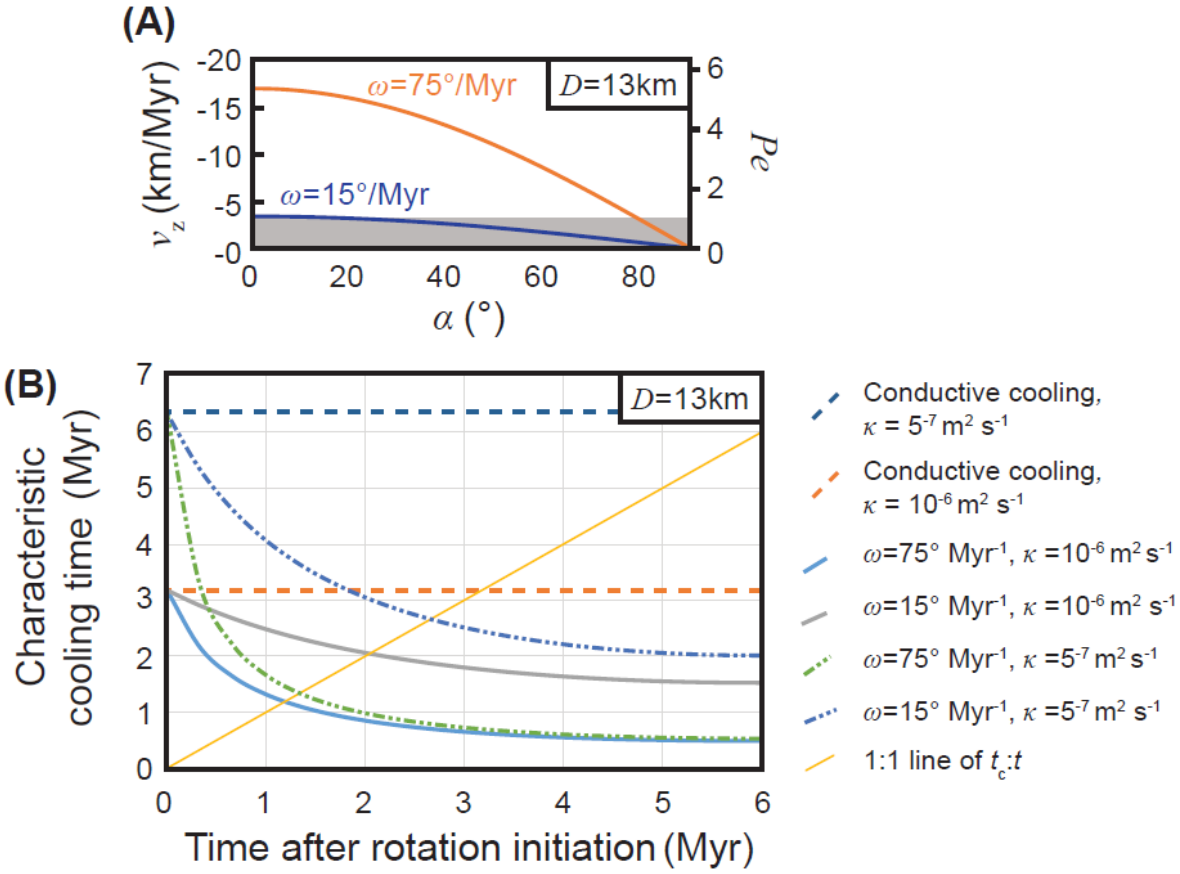

Figure 16. Vertical velocity (v_y) as a function of rotation angle (α), for two rotation rates (i.e., 15° Myr^{-1} and 75° Myr^{-1}), assuming D=13 km. The corresponding Péclet number (Pe) is shown on the right axis; gray shading represents $Pe \leq 1$, when conductive cooling dominates.

Table 1. Distinguishing features of the Searchlight pluton's units and ages

	Upper Searchlight		Middle Searchlight		Lower Searchlight		
Units label	Tsu	Tsu	Tsmul	Tsm	Tslu	Tsll	Tsld
Description	Quartz monzonite	Porphyritic qtz monzonite	Leucogranite	Granite	Quartz monzonite	Quartz monzonite	Ductilely deformed monzodiorite
Distinguishing texture		Porphyritic and equigranular		Weathered and "crunchy"; ~0.5 cm grains; less mafic than Tslu	Obvious 1-2 mm sphene; less kspar than Tsll	Kspar megacrysts	Strong foliation and more mafic minerals
Ages*	16.7-16.2Ma		16.2-16.0 Ma		16.3-16.1 Ma	17.7-16.3 Ma	-

*Age data from Bachl et al. (2001), Miller et al. (2006), and Faulds et al. (2010).

Table 2. (U-Th)/He zircon results and sample details

Sample	Unit	Latitude (°N)	Longitude (°W)	Elevation (m)	R* (km)	ZHe age (Ma)	2σ (Ma)
13-4C	Ts_{ll}	35.52691	114.81745	808	11.9	13.9	1.1
15-2	Ts_{ld}	35.56765	114.78263	663	16.4	12.3	1.0
14-9	Ts_{m}	35.50838	114.83319	893	10.1	16.4	1.3
14-4	Ts_{ll}	35.55199	114.82181	915	12.3	14.1	1.3
SLP1	$Ts_{ll}^{@}$	35.50548	114.75472	494	16.7	13.3	1.0
SLP2	Ts_{m}	35.53408	114.84011	959	10.2	13.1	1.5
14-5	Ts_{ll}	35.55256	114.82245	927	12.4	13.0	1.0

*R is the distance of the sample from the roof of the pluton, plus 2 km for the thickness of the overlying volcanic rocks, along a line trending N73°E.

@Sample SLP1 is a dike, with a composition similar to Ts_{ll}, intruding the Proterozoic basement rocks.

Table 3. Comparison of different models for observations across the Searchlight pluton

	Explanations based on Models		
Observation	Rigid-body rotation	Imbrication	Flow-like rotation
Up to 90° westward tilting	Rigid-body rotation of the pluton during listric or domino faulting	Semi-rigid body rotation with late-stage west-dipping antithetic faults	Flow-like rotation due to hanging wall removal
Slip on Dupont Mountain fault	Large magnitude (>10 km) to expose the base of the pluton	Large magnitude (>10 km) to expose the base of the pluton	Large magnitude (>10 km) to expose the base of the pluton
Slip on McCullough Range fault	Large magnitude (>10 km) to accommodate rotation of the pluton in its hanging wall	Large-to-medium magnitude (~10 km) to accommodate rotation of the pluton, but antithetic faulting reduces required magnitude	Lower magnitude (≤5 km) required
Eastside-up sub-solidus shear (top-west in pre-tilting reference frame)	Distributed top-west simple shear prior to pluton tilting	A combination of top-west simple hear prior to pluton tilting and antithetic shear zones that facilitate rotation	Flow results from velocity gradient during footwall flow toward the surface